



NTNU – Trondheim
Norwegian University of
Science and Technology

Terahertz Time-Domain Spectroscopy of Thin Material Samples

Trygve Reinertsen Sörgård

Master of Science in Physics and Mathematics

Submission date: July 2015

Supervisor: Ursula Gibson, IFY

Co-supervisor: Ulf Lennart Österberg, NTNU/IET

Norwegian University of Science and Technology
Department of Physics

Terahertz time-domain spectroscopy of thin material samples.

Author:

Trygve Reinertsen Sørgård

Supervisor::

Ursula Gison

Professor, NTNU-IFY

Co-Supervisor:

Ulf Lennart Österberg

Professor, NTNU-IET



NTNU
Department
of Physics



NTNU
Department
of Electronics and
telecommunications

Abstract

This thesis describes the techniques used in terahertz time-domain spectroscopy to determine the optical properties of layers that are thin compared to the length of the terahertz pulse.

An iterative procedure is used to minimize the difference between the measured transfer function and the expression for a Fabry-Pérot etalon when calculating the complex refractive index, $\hat{n}(\omega) = n(\omega) + i\kappa(\omega)$, while simultaneously determining the thickness of the medium.

Measurements were performed on slabs of silicon with thicknesses of 50, 10 and 2 microns to test this approach. For all the samples, the determined thickness was larger than expected and the optical parameters deviated from the expected values. This could be caused by the rough surfaces of the samples, which are not accounted for in the models presented here.

Absorbing media were simulated using the finite-difference time-domain scheme to calculate a modeled THz pulse shape after propagation through thin layers. Use of these modeled pulse shapes allowed retrieval of the optical parameters and thickness in a self-consistent manner.

Sammendrag

Denne oppgaven omhandler målinger av den komplekse refraksjonsindeksen, $\hat{n}(\omega) = n(\omega) + i\kappa(\omega)$ til et materiale i terahertzregimet (0.3-7 THz) ved bruk av tidsdomenespektroskopi.

En iterative metode ble brukt til å minimisere forskjellen mellom den målte overføringsfunksjonen og et uttrykk for en Fabry-Pérot etalon for å beregne the komplekse refraksjonsindeksen samtidig som man bestemmer tykkelsen til materialet.

Målinger ble gjort på tynne silisiumskiver med tykkelse 50,10 og 2 mikrometer for å teste beregningsmetoden. For alle prøvene ble tykkelse funnet til å være tykkere enn de forventede verdiene. De optiske parametrene var også ulikt det som ble forventet. Dette kan skyldes at prøvene har ru overflater, noe som ikke er tatt med i beregningene.

Absorberende medier ble simulert ved bruk av finite-difference time-domain metoden for å beregne terahertzpulser som propagerer gjennom tynne medier. De modellerte pulsene gjorde det mulig å beregne både optiske parametre og tykkelsen til materialet.

Preface

This Master Thesis contains the work performed in the Ultrafast Optics laboratory at NTNU during the spring of 2015.

I would like to thank my advisors, professors Ursula Gibson and Ulf Lennart Österberg. Both have been extremely helpful and have helped form this thesis in the best way possible considering all the bumps in the road towards getting here. I would like to thank Ulf especially for his help in the lab. His dedication and genuine interest in what he does is truly inspiring. He has been a great mentor, motivator and friend during the many hours spent doing measurements.

I would also like to thank all the people that have helped me by reading through this thesis during the writing process. Lastly, I'd like to thank my classmates for five fantastic years at NTNU.

Nomenclature

Abbreviations

BBO	β -Barium Borate
BS	Beam-splitter
c.c.	Complex conjugate
DFG	Difference-Frequency Generation
FDTD	Finite-Difference Time-Domain
FP	Fabry-Pérot
GaP	Gallium Phosphide
ITO	Tin doped Indium Oxide
OR	Optical Rectification
PC	Photonic Crystal
SFG	Sum-Frequency Generation
SHG	Second Harmonic Generation
Si	Silicon
TDS	Time-Domain Spectroscopy
THz	Terahertz

Symbols

μ_0	Permeability in free space
ϵ_0	Permittivity in free space
\vec{E}	Electrical field strength
\vec{M}	Magnetic field strength
\vec{D}	Displacement field strength
\vec{P}	Polarization
χ	Electric susceptibility
σ	Electric conductivity
σ^*	Magnetic conductivity

$\hat{n}(\omega)$	Complex index of refraction
$n(\omega)$	Refractive index
$\kappa(\omega)$	Extinction coefficient
$\alpha(\omega)$	Absorption coefficient
α	Polarizability
γ	Damping constant
ω_0	Resonance frequency
τ	Relaxation time
ϵ_s	Static permittivity
ϵ_∞	High-frequency permittivity

Contents

1	Introduction	1
2	Theory	3
2.1	Fundamentals of electromagnetics	3
2.2	Electromagnetic interactions with dispersive media.	6
2.2.1	The Lorentz model	6
2.2.2	The Debye model for dielectric relaxation	8
2.3	Reflection and transmission at interfaces	11
2.3.1	Fabry-Perot etalon.	13
2.4	Generation and detection of THz pulses	14
2.4.1	Photoconductive antenna	15
2.4.2	Optical rectification	16
2.4.3	THz generation in air	18
2.4.4	Electro-optic detection	18
3	Terahertz time-domain spectroscopy	23
3.1	Measuring with terahertz time-domain spectroscopy	23
3.2	Calculating the optical parameters.	24
4	Simulation methods	31
4.1	Finite Difference Time Domain algorithm	31
4.2	Dispersion	33
4.2.1	Debye medium	34
4.2.2	Lorentz medium	35
5	Experimental methods	37
5.1	Experimental setup	37
5.2	Assumptions and uncertainties	39
5.2.1	Signal to noise ratio and dynamic range	40
6	Results	43
6.1	Measurements	43
6.1.1	50 micron silicon sample	43
6.1.2	10 micron silicon sample	47
6.1.3	2 micron silicon sample	49
6.2	Simulations	51

6.2.1	Lorentz medium	53
6.2.2	Debye medium	54
7	Discussion	55
7.1	Errors in the minimization method	55
7.1.1	Choice of initial guess	56
7.2	Measured samples	56
7.2.1	50 micron silicon sample	57
7.2.2	10 micron silicon sample	58
7.2.3	2 micron silicon sample	58
7.3	Simulations	59
8	Conclusion and further work	61
A	The Nelder-Mead Simplex method	63
B	An interesting phenomenon	67
C	Sign conventions	69
	Bibliography	71

Chapter 1

Introduction

Terahertz radiation, or T-rays, is electromagnetic radiation with frequencies in the range of $10^{11} - 10^{13}$ Hz, in between the infrared and microwave regions of the electromagnetic spectrum. During the last two decades, THz technology has become involved in disciplines such as ultrafast spectroscopy, security applications,¹ and bio-medical imaging.² In THz technology the material response to an external electromagnetic field is studied. Rotational transitions of molecules,³ large-amplitude vibrational modes of organic compounds, lattice vibrations in solids,⁴ intraband transitions in semiconductors and energy gaps in superconductors are all examples of interactions between electromagnetic waves and matter in the THz-region. For instance, rotational transitions of water vapor molecules couple strongly with THz radiation. This causes a lot of the THz radiation to be absorbed when propagating through air, i.e. there is high atmospheric opacity for THz-radiation. This fact, on the one hand, severely limits the range of THz applications. On the other hand, because of its strong attenuation in water, it is possible to use THz radiation to detect anomalies or defects through small variations in the amount of water in a system. Physical values of THz radiation at frequency 1 THz is shown in table 1.1.

TABLE 1.1: Physical values of radiation at frequency $\nu = 1$ THz.

Physical quantity	Relation	Values in SI units
Wavelength	$\lambda = c/\nu$	0.3 mm = 300 μm
Period	$\tau = 1/\nu$	10^{-12} s = 1 ps
Photon energy	$E = h\nu$	4.14 meV
Temperature	$T = h\nu/k_B$	48 K

Terahertz time-domain spectroscopy (THz-TDS) is a powerful tool for measuring the optical parameters of a material within a wide range of frequencies. In this thesis, the focus lies on measuring very thin material samples. When measuring thin samples, the Fabry-Pérot reflections must be included in the calculations of the optical parameters. In such cases iterative methods are required to retrieve the optical parameters. The interaction

between THz pulses and thin material samples has been further investigated by a simulation using the finite-difference time-domain (FDTD) scheme.

Material characterization and cataloging with THz-TDS is very important in for future developments of THz applications, such as waveguides, polarizers and metamaterials, such as photonic crystals.

In the next chapter some basic principles of electromagnetic theory will be presented as well as some theory concerning the interaction between electromagnetic waves and matter. The theory chapter also presents some principles for generation and detection of THz pulses. In chapter 3, the principles of terahertz time-domain spectroscopy are explained. Chapter 4 features an introduction to the Finite-Difference Time-Domain algorithm for simulation of the propagation of electromagnetic pulse. The simulations shown in this chapter will add to our understanding of how the THz pulse interacts with different materials. Chapter 5 is a description of how the measurements were conducted, and what assumptions have to be made in order to be able to extract data from the measurements. The measurement data and results are presented in chapter 6. In chapter 7 we discuss the results found by the measurements and the simulataions. Chapter 8 Summarizes the findings, and discusses what could be done as part of future work to handle any problems found throughout the discussion.

Chapter 2

Theory

This chapter covers some general principles of electromagnetic theory, such as the wave equation and the Fresnel equations. These will make it easier to understand how light interacts with matter. A brief explanation will be given on the properties of the Fabry-Perot etalon. This chapter also covers some basic techniques for generation and detection of THz radiation. Most of the theory presented here can be found in 'Nonlinear Optics' by R. Boyd⁵ and 'Principles of Terahertz Science and Technology' by Y.-S. Lee.⁶ Additional references are given throughout the chapter when needed.

2.1 Fundamentals of electromagnetics

The entire theoretical basis of classical electrodynamics consists of Maxwell's equations

$$\nabla \cdot \vec{D} = \rho_f, \quad (2.1)$$

$$\nabla \cdot \vec{B} = 0, \quad (2.2)$$

$$\nabla \times \vec{E} = -\frac{\partial \vec{B}}{\partial t}, \quad (2.3)$$

$$\nabla \times \vec{H} = \vec{J}_f + \frac{\partial \vec{D}}{\partial t}, \quad (2.4)$$

and the Lorentz force law

$$\vec{F} = q(\vec{E} + \vec{v} \times \vec{B}), \quad (2.5)$$

where \vec{E} and \vec{B} are the electric and magnetic field that constitute electromagnetic radiation and ρ_f and \vec{J}_f are the free charges and currents in the medium. The electric displacement field \vec{D} and the magnetic field \vec{H} are

related to the fundamental fields by

$$\vec{D} \equiv \epsilon_0 \vec{E} + \vec{P} = \epsilon_0(1 + \chi) \vec{E} = \epsilon \vec{E}, \quad (2.6)$$

$$\vec{H} \equiv \frac{1}{\mu_0} \vec{B} - \vec{M} = \frac{1}{\mu} \vec{B}, \quad (2.7)$$

where ϵ, μ, \vec{P} and \vec{M} are the electric permittivity, the permeability, the polarization and the magnetization of the material, respectively. The subscript 0 (see ϵ_0) denotes the physical value of a system in vacuum. In most cases, non-magnetic materials are considered, i.e. materials where $\vec{M} = 0$, so that $\mu = \mu_0$. χ is the electric susceptibility of the material. It is related to the relative permittivity of the system by the relation

$$\epsilon_r = \frac{\epsilon}{\epsilon_0} = 1 + \chi. \quad (2.8)$$

For convenience we can express the polarization as a linear and a non-linear term:

$$\begin{aligned} \vec{P} &= \vec{P}^{(1)} + \vec{P}^{(2)} + \vec{P}^{(3)} + \dots \\ &= \vec{P}^{(1)} + \vec{P}^{(\text{NL})}, \end{aligned} \quad (2.9)$$

so that the displacement field can be expressed as

$$\begin{aligned} \vec{D} &= \epsilon_0 \vec{E} + \vec{P}^{(1)} + \vec{P}^{(\text{NL})} \\ &= \epsilon_0 \epsilon^{(1)} \cdot \vec{E} + \vec{P}^{(\text{NL})}, \end{aligned} \quad (2.10)$$

where $\epsilon^{(1)}$ is a dielectric tensor, which reduces to a scalar for isotropic media. We can assume that \vec{J}_f is linear with the electric field. This is for example a good approximation for metals, where the dependence on \vec{J} on \vec{E} is well described by the Drude model of electrical conduction. We also assume that we can neglect free charges, i.e.

$$\vec{J}_f = \sigma \vec{E}, \quad (2.11)$$

$$\rho_f = 0, \quad (2.12)$$

where σ is the electric conductivity of the medium. By taking the curl of eq. (2.3) and using the relations found in eqs. (2.6) and (2.7) we find

$$\nabla^2 \vec{E} - \nabla(\nabla \cdot \vec{E}) = \epsilon_0 \epsilon^{(1)} \mu_0 \frac{\partial^2 \vec{E}}{\partial t^2} + \mu_0 \sigma \frac{\partial \vec{E}}{\partial t} + \mu_0 \frac{\partial^2 \vec{P}^{(\text{NL})}}{\partial t^2}. \quad (2.13)$$

In a homogeneous medium, the second term on the left hand side is zero due to the fact that $\nabla \cdot \vec{D} = 0$. This implies that $\nabla \cdot \vec{E} = 0$. We are therefore left with

$$\nabla^2 \vec{E} = \sigma \mu_0 \frac{\partial \vec{E}}{\partial t} + \epsilon^{(1)} \epsilon_0 \mu_0 \frac{\partial^2 \vec{E}}{\partial t^2} + \mu_0 \frac{\partial^2 \vec{P}^{(NL)}}{\partial t^2}. \quad (2.14)$$

The nonlinear polarization plays a key role in many process for generation of THz radiation, e.g. through a process known as optical rectification, which will be discussed further in section 2.4.2. For a linear dielectric medium with no conductivity, $\sigma = 0$, and $\epsilon^{(1)} = \hat{n}^2$, where \hat{n} is the complex index of refraction, we obtain the wave equation in its simplest form

$$\nabla^2 \vec{E} = \frac{1}{v^2} \frac{\partial^2 \vec{E}}{\partial t^2}, \quad (2.15)$$

where $v = c/\hat{n}$ is the phase velocity of the wave within the medium and $\epsilon_0 \mu_0 = 1/c^2$. One solution of this equation is a linearly polarized monochromatic wave. As an example, consider such a wave propagating in z -direction with frequency ω :

$$E(z, t) = E_0 e^{i(kz - \omega t)}. \quad (2.16)$$

The wave-number, k is related to the aforementioned complex refractive index \hat{n} by the relation

$$k = \frac{2\pi \hat{n}}{\lambda_0} = \frac{2\pi \nu \hat{n}}{c_0} = \frac{\omega \hat{n}}{c_0} \quad (2.17)$$

where λ_0 , c_0 and ν are the wavelength in vacuum, the speed of light in vacuum and the frequency, respectively. $\omega = 2\pi\nu$ is the angular frequency. The complex refractive index is frequency dependent and describes the optical properties of the material. It can be expressed as

$$\hat{n}(\omega) = n(\omega) + i\kappa(\omega) = n(\omega) + i \frac{\alpha(\omega)c}{2\omega}, \quad (2.18)$$

where $n(\omega)$ is the refractive index, indicating the phase velocity, $\kappa(\omega) \geq 0$, is the extinction coefficient and $\alpha(\omega)$ is the absorption coefficient, which indicates the amount of absorption loss when the wave propagates through the medium. The reason some people like to write α instead of κ is that κ has units 1, while α has units m^{-1} , and thereby gives a measure of how large the absorption is for a unit of length. The solution of eq. (2.15) has the form

$$E(z, t) = E_0 e^{i\omega(n(\omega)z/c - t)} e^{-\omega\kappa(\omega)z/c} \quad (2.19)$$

$$= E_0 e^{i\omega(n(\omega)z/c - t)} e^{-\alpha(\omega)z/2}. \quad (2.20)$$

2.2 Electromagnetic interactions with dispersive media.

The way a medium reacts to external electromagnetic radiation is characterized by dispersion and absorption, i.e. $n(\omega)$ and $\kappa(\omega)$. All electromagnetic phenomena involve interactions between electromagnetic fields and charged particles. An electromagnetic wave can cause charged particles to move, which in turn causes the particles to radiate. In an absorptionless medium, $\kappa = 0$. The intensity of the light is not reduced as it passes through this sort of medium. In a dispersive medium, different frequencies of light travel at different speeds. They are also refracted differently at the materials surface. Sunlight refracting and reflecting in dispersive water bubbles is what causes a rainbow to appear in the sky. Some materials even have resonances, which makes them react strongly to light of specific frequencies. Some of these materials can be described by simple models, which will be explained in this section.

2.2.1 The Lorentz model

The Lorentz model describes the electrons in a medium as driven harmonic oscillators. Since the electrons are much, much lighter than the nuclei, we can assume that the nuclei are at rest. In this model the electron is connected to the nucleus as a mass on a spring connected to a wall. In the presence of a monochromatic wave the oscillator is described as

$$\ddot{x} + \gamma\dot{x} + \omega_0 x = \frac{q}{m} E_0 e^{-i\omega t}, \quad (2.21)$$

where x is the electrons displacement from equilibrium, γ is a damping constant, ω_0 is the resonance frequency of the electron and q and m is the charge, and mass of the electron, respectively. The external monochromatic field has amplitude E_0 and driving frequency ω . The solution of this equation for the displacement of the electron is

$$x(t) = \frac{q}{m} \frac{E_0 e^{-i\omega t}}{\omega_0^2 - \omega^2 - i\gamma\omega}. \quad (2.22)$$

The oscillating charges in the medium carry an electric dipole moment

$$p(t) = qx(t). \quad (2.23)$$

For a number of atoms, N , the bulk polarization induced in the medium by the electric field is

$$P(t) = Np(t) = \epsilon_0 \chi E_0 e^{-i\omega t}. \quad (2.24)$$

From the relations eqs. (2.6) and (2.8), the relative permittivity can be expressed as

$$\epsilon_r(\omega) = 1 + \chi(\omega) = 1 + \frac{Nq^2}{m\epsilon_0} \frac{1}{\omega_0^2 - \omega^2 - i\gamma\omega}. \quad (2.25)$$

This expression can be expressed by the high-frequency and the static limit ($\omega \mapsto \infty$ and $\omega \mapsto 0$) as

$$\epsilon_r(\omega) = \epsilon_\infty + \frac{\omega_0^2(\epsilon_s - \epsilon_\infty)}{\omega_0^2 - \omega^2 - i\gamma\omega}, \quad (2.26)$$

where $\epsilon_\infty = 1$ is the high-frequency limit and $\epsilon_s = 1 + \omega_0^2 Nq^2 / \epsilon_0$ is the static limit. The real and imaginary parts of ϵ_r are related to the complex refractive index by the relations

$$n^2 = \frac{1}{2}(\Re(\epsilon)^2 + \Im(\epsilon)^2)^{1/2} + \frac{\Re(\epsilon)}{2} \quad (2.27)$$

$$\kappa^2 = \frac{1}{2}(\Re(\epsilon)^2 + \Im(\epsilon)^2)^{1/2} - \frac{\Re(\epsilon)}{2}. \quad (2.28)$$

The frequency dependences of the real and imaginary parts of the relative permittivity are shown in Fig. 2.1. The real and imaginary parts of $\hat{n} = n + i\kappa$ have the same forms as ϵ' and ϵ'' .

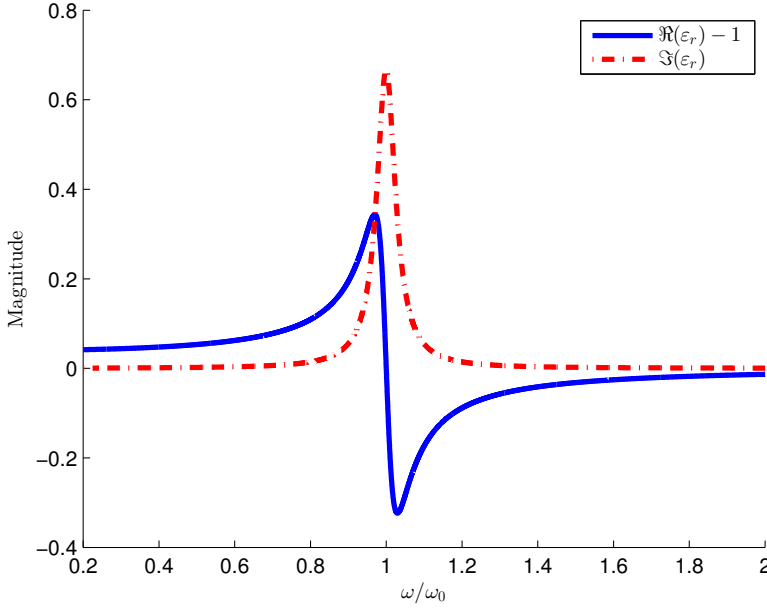


FIGURE 2.1: The real and imaginary parts of the relative permittivity. The real and imaginary parts of the refractive index have the same shapes. The plot is made with a damping term $\gamma = 0.3$ and the term $Nq^2/m\epsilon_0$ has been set to 1. Decreasing γ increases the magnitude of the resonance peak.

2.2.2 The Debye model for dielectric relaxation

When an electric field is applied to a material, it does not become instantly polarized. In the time domain we express the polarization as

$$\vec{P}(t) = \epsilon_0 \int_{-\infty}^t \chi(t-t') \vec{E}(t') dt', \quad (2.29)$$

which by the convolution theorem leads to

$$\vec{P}(\omega) = \epsilon_0 \chi(\omega) \vec{E}(\omega). \quad (2.30)$$

In analogy, the material does not instantly revert back to equilibrium when the applied field is turned off. For a polarization, $\vec{P} = N\alpha\vec{E}$, where α is the polarizability, N is the number of atoms and \vec{E} is the external electric field,

the simplest equation of motion for the polarization is given by⁷

$$\tau dP(t)/dt + P(t) = N\alpha E(t). \quad (2.31)$$

If the external electric field is removed it is easily seen that the polarization within the material decays exponentially

$$P(t) = P(0)e^{-t/\tau}. \quad (2.32)$$

τ is called the Debye relaxation time. The exponential decay of the polarization in the material is called the Debye relaxation process. In the presence of the external electric field eq. (2.31) is of the form

$$\dot{y}(t) = \tau^{-1}a(t) - \tau^{-1}y(t), \quad (2.33)$$

which has the general solution

$$y(t) = e^{-t/\tau} \left[y(-\infty) + \tau^{-1} \int_{-\infty}^t a(t') e^{t'/\tau} dt' \right]. \quad (2.34)$$

We assume that the polarization disappears after the electric field vanishes, so we can set $P(-\infty) = 0$. If we assume that the electric field is of the form $E(t) = E(\omega)e^{-i\omega t}$, the integral can be solved analytically:

$$P(t) = NE(\omega)e^{-t/\tau} \alpha \tau^{-1} \int_{-\infty}^t a(t') e^{t'(1/\tau - i\omega)} dt' \quad (2.35)$$

$$= \frac{NE(\omega)\alpha\tau^{-1}e^{-i\omega t}}{\tau^{-1} - i\omega} \quad (2.36)$$

$$= \frac{NE(\omega)\alpha}{1 - i\omega\tau} e^{-i\omega t}. \quad (2.37)$$

The fourier transform of the polarization becomes

$$P(\omega) = \frac{NE(\omega)\alpha}{1 - i\omega\tau} = \chi(\omega)E(\omega), \quad (2.38)$$

so the dielectric constant, ϵ , becomes

$$\epsilon = 1 + \chi = 1 + \frac{N\alpha}{1 - i\omega\tau} \quad (2.39)$$

$$= 1 + \frac{N\alpha}{1 + (\omega\tau)^2} + i \frac{N\alpha\omega\tau}{1 + (\omega\tau)^2} \quad (2.40)$$

The dielectric constant is usually expressed in terms of the zero frequency and high frequency dielectric constants, ϵ_0 and ϵ_∞ ,

$$\epsilon(\omega) = \epsilon_\infty + \frac{\epsilon_s - \epsilon_\infty}{1 - i\omega\tau} \quad (2.41)$$

The real and imaginary parts of the dielectric constant can now be expressed as

$$\epsilon_r(\omega) = \epsilon_\infty + \frac{\epsilon_s - \epsilon_\infty}{1 + (\omega\tau)^2} \quad (2.42)$$

$$\epsilon_i(\omega) = \frac{(\epsilon_s - \epsilon_\infty)\omega\tau}{1 + (\omega\tau)^2}. \quad (2.43)$$

Many materials exhibit multiple relaxation processes. The easiest way to describe these is to assume multiple first-order processes, resulting in a sum of Debye processes.

$$\epsilon(\omega) = \epsilon_\infty + \sum_{j=1}^N \frac{\Delta\epsilon_j}{1 - i\omega\tau_j}, \quad (2.44)$$

where $\Delta\epsilon_j = \epsilon_j - \epsilon_{j+1}$. The static term, ϵ_s is the same as ϵ_1 . ϵ_j is an intermediate-frequency term. A medium can also have multiple Lorentz-resonances, or even both Lorentz and Debye terms. As an example, consider the two-term Debye equation for water,

$$\epsilon(\omega) = \epsilon_\infty + \frac{\epsilon_s - \epsilon_2}{1 - i\omega\tau_1} + \frac{\epsilon_2 - \epsilon_\infty}{1 - i\omega\tau_2}, \quad (2.45)$$

where ϵ_2 is an intermediate frequency limit. τ_1 and τ_2 describe the slow and fast relaxation processes of water, respectively. Figure 2.2 shows the real and imaginary parts for the Debye equation for water in the THz regime.

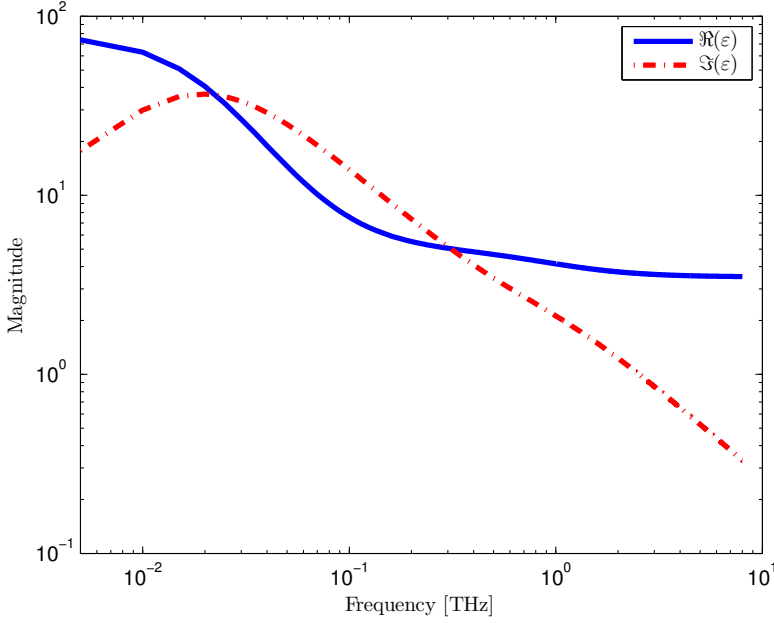


FIGURE 2.2: The real and imaginary parts of the dielectric permittivity for water. The values are: $\epsilon_\infty = 3.5$, $\epsilon_s = 78.4$, $\epsilon_2 = 4.9$, $\tau_1 = 8.2$ ps and $\tau_2 = 0.18$ ps.⁸

2.3 Reflection and transmission at interfaces

From Maxwell's equations it can be shown that the boundary conditions for the electric and magnetic field incident on a *linear* dielectric medium are

$$E_1^\parallel = E_2^\parallel, \quad (2.46)$$

$$\epsilon_1 E_1^\perp = \epsilon_2 E_2^\perp, \quad (2.47)$$

$$\frac{1}{\mu_1} B_1^\parallel = \frac{1}{\mu_2} B_2^\parallel, \quad (2.48)$$

$$B_1^\perp = B_2^\perp, \quad (2.49)$$

where the subscripts 1 and 2 denote the fields on each side of the interface and the superscript symbols \parallel and \perp denote the components of the fields that are parallel and perpendicular to the boundary, respectively. The direction of the electric field is commonly referred to as the polarization

of the radiation. The cases of plane electromagnetic waves with different polarization incident on a flat surface are shown in Fig. 2.3. The light is defined as either p-polarized or s-polarized when the electric field of the incident wave is parallel and perpendicular, respectively, to the plane of incidence (i.e. the plane which contains the surface normal and the propagation vector \vec{k} of the incident field). The "s" stands for "senkrecht", which is the German word for perpendicular. For p-polarization, the electric field lies in the plane of incidence and its components are both parallel and perpendicular to the boundary, while for s-polarization all components of the electric field are parallel to the boundary.

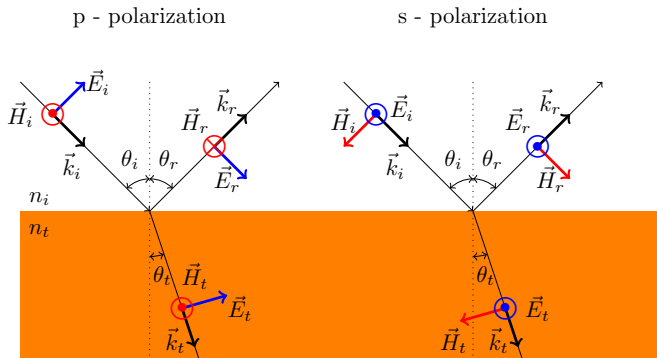


FIGURE 2.3: **p-polarization:** The Electric field (blue) lies in the plane of incidence. **s-polarization:** The Magnetic field (red) lies in the plane of incidence.

The subscripts i, r , and t in Fig. 2.3 stand for incident, reflected and transmitted, respectively. The angles θ_i, θ_r and θ_t are the angles between the propagation vectors for the incident, reflected and transmitted light, and the surface normal. The angles are related by

$$\theta_i = \theta_r, \quad (2.50)$$

$$n_i \sin \theta_i = n_t \sin \theta_t, \quad (2.51)$$

where the last of these two equations is known as Snell's law. The boundary conditions determine the ratios of the reflected and transmitted field amplitudes to the incident field amplitude. These relations are known as the

Fresnel equations

$$r^s = \frac{E_r^s}{E_i^s} = \frac{n_i \cos \theta_i - n_t \cos \theta_t}{n_i \cos \theta_i + n_t \cos \theta_t}, \quad t^s = \frac{E_t^s}{E_i^s} = \frac{2n_i \cos \theta_i}{n_i \cos \theta_i + n_t \cos \theta_t}, \quad (2.52)$$

$$r^p = \frac{E_r^p}{E_i^p} = \frac{n_t \cos \theta_i - n_i \cos \theta_t}{n_t \cos \theta_i + n_i \cos \theta_t}, \quad t^p = \frac{E_t^p}{E_i^p} = \frac{2n_i \cos \theta_i}{n_t \cos \theta_i + n_i \cos \theta_t}. \quad (2.53)$$

We define the reflected and transmitted power as

$$R = |r|^2, \quad (2.54)$$

$$T = \frac{n_t}{n_i} |t|^2. \quad (2.55)$$

2.3.1 Fabry-Perot etalon.

When light enters a material, some of it is reflected and some of it passes into the medium. At the other end of the sample, the same thing happens. The reflecting material surfaces constitute the Fabry-Pérot etalon. As light propagates back and forth within the sample, some parts of the light is let out each time it collides with the sample surface. The pulses of light from each collision with the sample surface are called Fabry-Pérot reflections or multiple reflections. Figure 2.4 shows the electromagnetic field being reflected and refracted at an angle at both interfaces of a sample. The angles between the surface normal and the propagation direction of light are renamed θ outside the sample and β inside the sample, in order to avoid subscripts.

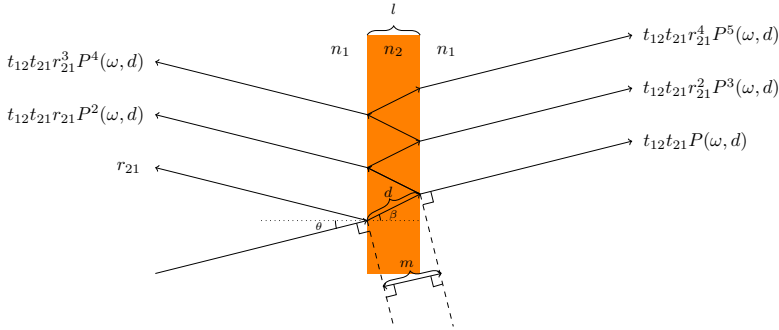


FIGURE 2.4: Multiple reflections and transmissions of an electromagnetic wave passing through a medium.

The transmitted electric field can be expressed as the sum of multiple reflections.

$$E_t(\omega) = E_i(\omega)t_{12}P(\omega, d)t_{21} + E_i(\omega)t_{12}P(\omega, d)^3r_{21}^2t_{21} \\ + E_i(\omega)t_{12}P(\omega, d)^5r_{21}^4t_{21} + \dots \quad (2.56)$$

$$= E_i(\omega)t_{12}P(\omega, d)t_{21} \sum_{\delta=0}^{\delta=\infty} P(\omega, d)^\delta r_{21}^\delta \quad (2.57)$$

$$= E_i(\omega)t_{12}P(\omega, d)t_{21} \frac{1}{1 - (P(\omega, d)r_{21})^2} \quad (2.58)$$

where $P(\omega, d) = \exp[-i\hat{n}\omega d/c]$ is the propagation coefficient over a distance, $d = l/\cos\beta$, within the medium. The distance the pulse would have propagated through air if the sample wasn't there is $m = d \cos(\theta - \beta)$, where $\theta \geq \beta$. The coefficients t_{12}, t_{21}, r_{12} and r_{21} are the frequency-dependent Fresnel coefficients.

When light passes into the medium, the phase velocity, v , and the wavelength of the light, λ , are altered due to the change in the refractive index, n , of the medium. If the thickness of the sample equals an integer number of halfwavelengths, the light with these wavelengths (within the medium) will completely pass through the sample.

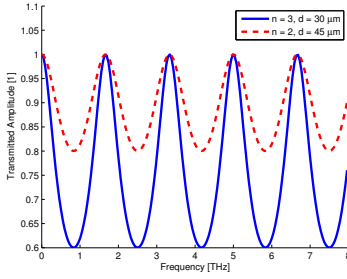
$$v = c_0/n \quad (2.59)$$

$$\lambda = \lambda_0/n \quad (2.60)$$

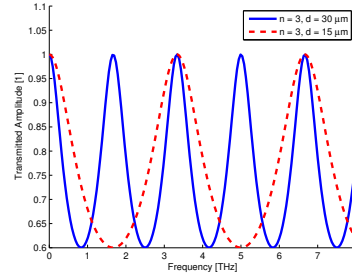
where c_0 and λ_0 is the speed of light and the wavelength in vacuum respectively. The frequency of the light remains the same within the medium as it is in vacuum. Figure 2.5 shows the transmitted intensity for different cases. We see that a thicker medium will allow light of more frequencies to completely pass through due to the fact that the thickness coincides with more half-lengths of wavelengths. Another thing to take note of is the fact that the dips between the transmission peaks are steeper for higher refractive indices due to the fact that more light is reflected on a surface with higher refractive index. The completely transmitted frequencies become more distinct compared as the reflectivity increases. A Fabry-Pérot etalon with high reflectivity is said to have high *finesse*.

2.4 Generation and detection of THz pulses

In several schemes for generation of broadband THz radiation, the electric field in the time domain takes the shape of nearly single-cycle pulses. Some



(a) Samples with the same optical thickness, but with different refractive indices and physical lengths.



(b) Samples with the same refractive index, but different thicknesses.

FIGURE 2.5: Transmitted intensities through different Fabry-Pérot etalons.

of the methods used to generate and detect such pulses will be explained in this section.

2.4.1 Photoconductive antenna

A Photoconductive (PC) antenna is an electrical switch based on the production of electron-hole pairs in a semiconductor as a result of incident photons. The antenna consists of two metal electrodes embedded in a semiconductor with an applied DC-field between as shown in Fig. 2.6.

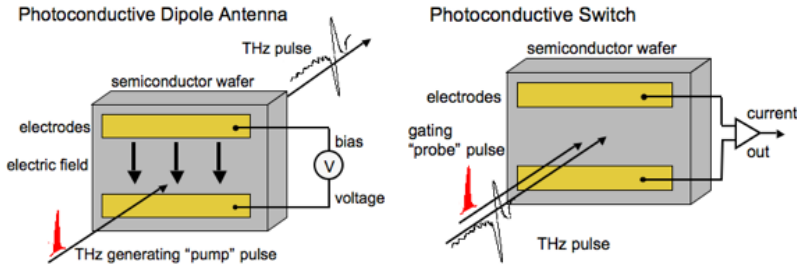


FIGURE 2.6: Photoconductive antenna and photoconductive switch.⁹

An incident optical pulse with photons whose energy is high enough to overcome the bandgap of the semiconductor creates electron-hole pairs between the electrodes embedded in the semiconductor. These pairs usually last shorter than the pulse duration (which is usually around 10-100 fs), before they are absorbed in the material. During their lifetime, the

electrons are accelerated by the DC bias field following eq. (2.5) creating a transient current $\vec{J}(t)$ and the induced polarization creates a time-dependent field opposing the DC field. The transient field acts as a source term for electromagnetic radiation

$$\nabla \times \vec{E}_{THz}(t) = -\mu \frac{\partial \vec{H}_{THz}(t)}{\partial t}, \quad (2.61)$$

$$\nabla \times \vec{H}_{THz}(t) = \vec{J}(t) + \frac{\partial \epsilon(t) \vec{E}_{THz}(t)}{\partial t}, \quad (2.62)$$

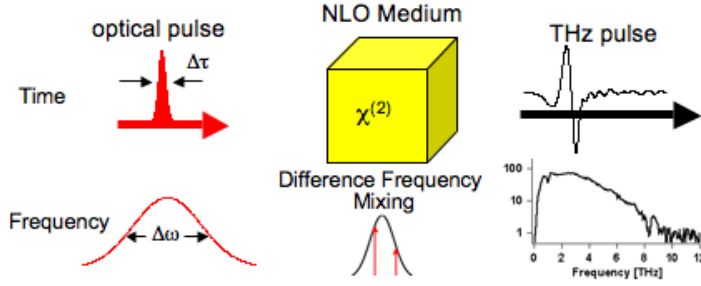
where $\vec{E}_{THz}(t)$ and $\vec{H}_{THz}(t)$ together constitute the radiated THz field. In the time-domain the radiated electric field will have an almost single-cycle form. Thus, in the frequency domain it will be a broadband pulse. When there is no longer any incoming optical pulse and the THz pulse has been radiated, the semiconductor recovers. THz radiation can be detected following the same principles as the generation. The geometry is shown on the right side of Fig. 2.6. Instead of a bias field between the electrodes, we measure the current due to charge movement occurring when a THz field and an optical pulse are present in the semiconductor at the same time; the optical pulse creates the carriers and the THz electric field accelerates them. The produced current is a convolution between the THz field and the transient surface conductivity σ_s ,

$$J(t) = \int_{-\infty}^t \sigma_s(t - \tau) E_{THz}(\tau) d\tau, \quad (2.63)$$

where t is the arrival time of the optical pulse. By varying the arrival time of the optical pulse we can measure the electric THz field as a function of time.

2.4.2 Optical rectification

Optical Rectification (OR) is a second-order non-linear optical effect which consists of the generation of DC electric polarization within a nonlinear medium as a result of an intense incident optical beam. The principal of THz generation through optical rectification is shown in Fig. 2.7: An optical pulse is incident on a nonlinear medium, in which the field aligns the electrons in such a way as to create a DC electric field within the medium. As the pulse intensity varies, so does the strength of the DC field. The varying field radiates a THz pulse.

FIGURE 2.7: Optical Rectification.⁹

The induced polarization of a material is described by

$$\begin{aligned} P(t) &= \epsilon_0 [\chi^{(1)} E(t) + \chi^{(2)} E^2(t) + \chi^{(3)} E^3(t) + \dots] \\ &\equiv P^{(1)}(t) + P^{(2)}(t) + P^{(3)}(t) + \dots, \end{aligned} \quad (2.64)$$

where $\chi^{(n)}$ is the n th-order susceptibility, where n is an integer number. The electric field is given by

$$E(t) = E'(t)e^{-i\omega t} + c.c. \quad (2.65)$$

where $E'(t)$ is the pulse envelope, ω is the carrier frequency and c.c. stands for the complex conjugate of the field, i.e. $E'^*(t)e^{+i\omega t}$. For a laser pulse with more than one distinct frequency component, the electric field and the resulting polarization can be expressed as

$$E(t) = E'_1(t)e^{-i\omega_1 t} + E'_2(t)e^{-i\omega_2 t} + c.c., \quad (2.66)$$

$$\begin{aligned} P(t) &= \epsilon_0 \chi^{(2)} [E_1'^2(t)e^{-2i\omega_1 t} + E_2'^2(t)e^{-2i\omega_2 t} + 2E'_1(t)E'_2(t)e^{-i(\omega_1 + \omega_2)t} \\ &\quad + 2E'_1(t)E_2'^*(t)e^{-i(\omega_1 - \omega_2)t} + c.c.] + 2\epsilon_0 \chi^{(2)} [E'_1(t)E_1'^*(t) + E'_2(t)E_2'^*(t)]. \end{aligned} \quad (2.67)$$

The terms oscillating at $2\omega_1$ and $2\omega_2$ are second harmonics of their respective input frequencies. This is known as Second Harmonic Generation (SHG). The terms oscillating at frequency $\omega_1 + \omega_2$ are known as a Sum-Frequency generated (SFG) terms since they oscillate at a frequency which is the sum of the two input frequencies. SHG is a special case of SFG, where $\omega_1 = \omega_2$. The terms oscillating at frequency $\omega_1 - \omega_2$ are known as a Difference-Frequency Generated (DFG) terms since they oscillate at a frequency which is the difference between the two input frequencies. Optical rectification is a special case of DFG, where $\omega_1 = \omega_2$, i.e. the difference frequency term becomes static. However, if the incident optical field is time-dependent, so is the optical rectification term, and a time-varying polarization leads to electromagnetic radiation and this property is used to generate THz pulses.

2.4.3 THz generation in air

In 1993 Hamster *et al.*¹⁰ first demonstrated the generation of THz waves through an intense laser-plasma interaction in air. They used a 800 nm wavelength pulse which, when focused generated a large density difference between ionic and electronic charges in the air. This happened because the pulse was short enough to inertially confine the ions. The ponderomotive forces involved in the charge separation resulted in a transient current. Later, Cook *et al.*¹¹ reported that a higher intensity THz-pulse could be generated by mixing the fundamental 800 nm pulse with its second harmonic, 400 nm in a third-order non-linear process known as four-wave mixing (FWM). This is the generation technique that we use for the experiments conducted in this thesis. The fundamental pulse is focused by a lens and passes through a type-I β -Barium Borate (BBO) crystal where the second harmonic is generated. The two waves interact at the focal point of the lens and creates a plasma. The THz radiation is generated from the transient photocurrent of the charges that are driven by the asymmetric fields of the superposition of the fundamental and the second harmonic. The generated THz field is proportional to the nonlinear current that arises, $J^{(3)}(t)$,

$$E_{THz}(t) \propto \frac{\partial}{\partial t} J^{(3)}(t). \quad (2.68)$$

The Fourier transform yields the relation

$$E_{THz}(\omega_T) \propto -i\omega_{THz} J^{(3)}(\omega_T) + c.c., \quad (2.69)$$

with

$$J^{(3)} = \sigma^{(3)} E_{2\omega} E_{\omega}^2 e^{-i\phi}, \quad (2.70)$$

where E_{ω} and $E_{2\omega}$ is the fundamental and the second harmonic, respectively, and ϕ is the phase difference between them. $\sigma^{(3)}$ is the third-order nonlinear conductivity. The result is that

$$E_{THz} \propto \sigma^{(3)} E_{2\omega} E_{\omega}^2 \sin(\phi). \quad (2.71)$$

2.4.4 Electro-optic detection

Electro-optic detection (EOD) exploits the same principles as optical rectification to directly measure the incident electric field of the THz pulse in the time-domain. The underlying mechanical effect is the Pockels effect: An electric field induces birefringence proportional to the input field in a

nonlinear crystal. The induced birefringence alters the polarization of the input field. By measuring the different polarization components we can determine the birefringence, and thus also the magnitude of the electric field. Pockels effect is a second-order nonlinear effect. The polarization can be expressed as

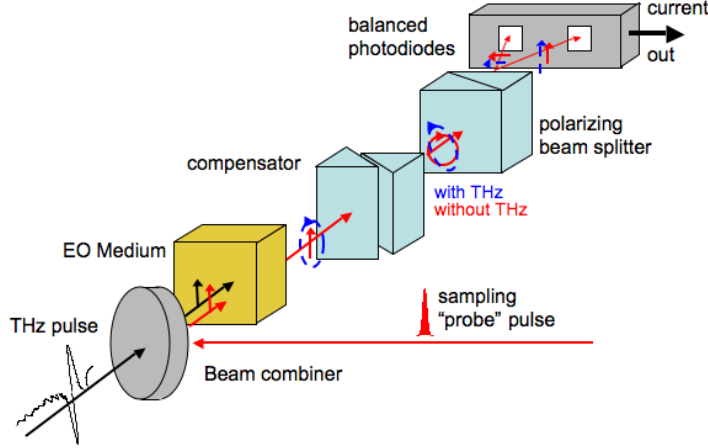
$$P_i^2(\omega) = 2 \sum_{j,k} \epsilon_0 \chi_{ijk}^{(2)}(\omega, \omega, 0) E_j(\omega) E_k(0) \quad (2.72)$$

$$= \sum_j \epsilon_0 \chi_{ij}^{(2)}(\omega) E_j(\omega), \quad (2.73)$$

where

$$\chi_{ij}^{(2)} = 2 \sum_k \chi_{ijk}^{(2)}(\omega, \omega, 0) E_k(0), \quad (2.74)$$

is the field induced susceptibility tensor. A schematic of the experimental setup for electro-optic detection is shown in Fig. 2.8: A THz pulse and a linearly polarized optical pulse are combined and are then incident on the electro-optic crystal. Depending on the strength of the THz pulse, the polarization of the combined pulse varies, e.g. if there is no THz pulse, the optical pulse remains linearly polarized. Then the pulse passes through a compensator, such as a quarter-wave plate; when there is no THz field, the optical pulse goes from linear to circular polarization. When there is a THz field, the combined pulse becomes elliptical. Thereafter, the pulse is split into two orthogonal components. If the pulse is circular, the components have the same magnitudes, if they are elliptical there is a difference in intensity, which can be measured by the balanced photodiodes.

FIGURE 2.8: Electro-optic detection.⁹

Let x and y be the crystal axes of the EO-crystal. When an electric field is applied to the EO-crystal, the axes of the electrically induced birefringence, x' and y' are at angle of 45° in relation to x and y . If the input light is propagating along the z -axis and is polarized along the x -axis, the output light after passing through the electro-optic crystal and the compensator can be expressed as¹²

$$\begin{pmatrix} E_x \\ E_y \end{pmatrix} = \begin{pmatrix} \cos(\pi/4) & -\sin(\pi/4) \\ \sin(\pi/4) & \cos(\pi/4) \end{pmatrix} \begin{pmatrix} \exp(i\delta) & 0 \\ 0 & 1 \end{pmatrix} \begin{pmatrix} \cos(\pi/4) & -\sin(\pi/4) \\ \sin(\pi/4) & \cos(\pi/4) \end{pmatrix} \begin{pmatrix} E_0 \\ 0 \end{pmatrix}, \quad (2.75)$$

where $\delta = \Gamma_0 + \Gamma$ is the phase difference between the x' and y' polarizations. Γ_0 is the static phase difference due to the intrinsic birefringence of the EO-crystal and the compensator, while Γ is the dynamic phase difference due to the birefringence induced by the applied THz field. The intensity is written as,

$$\begin{pmatrix} I_x \\ I_y \end{pmatrix} = \frac{1}{2} |E_0|^2 \begin{pmatrix} 1 + \cos(\delta) \\ 1 - \cos(\delta) \end{pmatrix} = I_0 \begin{pmatrix} \cos^2(\delta/2) \\ \sin^2(\delta/2) \end{pmatrix}. \quad (2.76)$$

Note that $I_x + I_y = I_0$, as long as there is no absorption in the electro optic crystal. The static term, Γ_0 , is also known as the optical bias, and is often set to $\pi/2$ for balanced detection. In most cases the dynamic phase term, Γ , is

very small, so we can write

$$\begin{pmatrix} I_x \\ I_y \end{pmatrix} = I_0 \begin{pmatrix} \cos^2(\pi/4 + \Gamma/2) \\ \sin^2(\pi/4 + \Gamma/2) \end{pmatrix} \quad (2.77)$$

$$= \frac{I_0}{2} \begin{pmatrix} 1 - \sin(\Gamma) \\ 1 + \sin(\Gamma) \end{pmatrix} \quad (2.78)$$

$$\approx \frac{I_0}{2} \begin{pmatrix} 1 - \Gamma \\ 1 + \Gamma \end{pmatrix}. \quad (2.79)$$

Now that the fundamental theory on electromagnetic interactions and terahertz pulses have been covered, it is time to move on to how one can perform measurements with a technique called terahertz time-domain spectroscopy, and how it can be used to determine the optical parameters of materials over a wide range of frequencies.

Chapter 3

Terahertz time-domain spectroscopy

This chapter explains the principles of performing measurement with terahertz time-domain spectroscopy and how to acquire knowledge of the optical parameters of the measured sample from the raw data.

3.1 Measuring with terahertz time-domain spectroscopy

Using devices for generating and detecting broadband THz pulses, one can measure changes in both amplitude and phase for the emitted pulse induced by a sample. In other words, we directly measure the THz electric field $E(t)$, not just the intensity $I(t) \propto |E(t)|^2$. Thus, we are provided enough information to determine the absorption and the refractive index of the sample simultaneously. This technique is called Terahertz Time-Domain Spectroscopy (THz-TDS).

When measuring a sample, two measurements are performed; One where the THz pulse passes through the setup undisturbed and one where the sample is placed along the pulse path. The reason for doing these two measurements is that by comparing the frequency spectra of the two pulses, it is possible to see how the material has affected the pulse. The pulse propagating through air will be referred to as the reference pulse and be denoted as E_r , while the pulse affected by the sample will be referred to as the sample pulse, E_s .

Measurements can be taken both in reflection mode and in transmission mode. In transmission mode it is enough to simply set the sample in the path of the THz pulse. The measured pulse will be delayed compared to the reference pulse. When performing THz-TDS in reflection mode the reference pulse is reflected by a mirror. It is crucial that the mirror and the sample surface are at the exact same distance from the emitter and are angled exactly the same so that the two pulses propagate over the same distance. This is difficult to achieve in any practical case, and may lead to some uncertainties in the phase shift. Hence, it is a lot easier to perform measurements in transmission mode. However, for samples with high absorption, it may be

impossible to perform measurements in transmission mode if the sample absorbs the THz pulse to such a degree that the signal is indistinguishable from noise. In order to perform transmission mode measurements of such samples, the sample must be sufficiently thin, so that the THz pulse is not attenuated to such a degree that it is distinguishable from the noise floor. Measuring thin samples causes additional complications since we are forced to include **Fabry-Pérot** reflections in our calculations. The experiments performed in this thesis are all in transmission mode.

3.2 Calculating the optical parameters.

To obtain knowledge of the optical parameters of the sample from the measurements, a Fourier transform is performed on the measured electric field,

$$E(\omega) = \int_{-\infty}^{\infty} E(t)e^{-i\omega t} dt. \quad (3.1)$$

When performing THz-TDS measurements, we distinguish between thin and thick samples, where a thick sample is thicker than the geometrical length of the incident pulse. This results in distinguishable Fabry-Pérot reflections. A thin sample, on the other hand, is thinner than the pulse's geometrical length.¹³ The reflections from a thin sample may overlap, causing the pulse to change shape. Another way of distinguishing between thick and thin samples is to require that the THz signal reaches zero between reflections for a thick sample.¹⁴ The pulse width has many definitions, but the most commonly used definition in experimental measurements is the Full-Width-Half-Maximum (FWHM), τ_{FWHM} , which is the time between the furthest separated points that have half of the pulse's peak intensity.¹⁵ The FWHM for the pulses in this experiment were $\tau_{FWHM} \approx 0.53$ ps. This corresponds to an optical thickness of ≈ 160 μm in vacuum. The pulse is compressed inside the medium by a factor equal to the refractive index. The optical thickness of a material is the product of the materials physical thickness and the index of refraction, $l_{opt} = nl$. For a thick sample, adjusting the measurement time to include only the first transmitted pulse is no trouble at all. In cases such as this, we can readily extract the sample's optical parameters by looking at the fourier transform of the single transmitted pulse,

$$E_s(\omega) = E_0(\omega)t_{12}t_{21}e^{i\hat{n}(\omega)\omega d/c}, \quad (3.2)$$

$$= E_0(\omega)t_{12}t_{21}e^{-\kappa(\omega)\omega d/c}e^{in(\omega)\omega d/c}, \quad (3.3)$$

$$= E_0(\omega)t_{12}t_{21}e^{-\alpha(\omega)d/2}e^{in(\omega)\omega d/c} \quad (3.4)$$

where $E_0(\omega)$ is the incident pulse, t_{12} and t_{21} are the frequency-dependent Fresnel coefficients from when the light passes into and out of the sample. By dividing the fourier transform of the pulse passing through a sample by the Fourier transform of a pulse passing through air, the complex transfer function $H(\omega)$ is obtained,

$$H(\omega) = \frac{E_s(\omega)}{E_r(\omega)} = T(\omega)e^{i\phi(\omega)} = t_{12}t_{21}e^{-\alpha(\omega)d/2}e^{i(n(\omega)d - n_{air}m)\omega/c}. \quad (3.5)$$

If we limit the analysis to normal incidence, the cosine terms in the Fresnel coefficients can be ignored and the propagation distances, m and d , for the reference and sample pulses can both be set to the thickness of the material, l . See Fig. 2.4. If the analysis is limited to materials with low absorption, the Fresnel coefficients are real-valued, and the equations are easily solved in order to obtain the complex refractive index,¹⁶

$$n(\omega) = 1 + \frac{\phi(\omega)c}{\omega l} \quad (3.6)$$

$$\alpha(\omega) = -\frac{2}{l} \ln \left(\frac{(n(\omega) + n_{air})^2}{4n(\omega)} T(\omega) \right). \quad (3.7)$$

When solving eqs. (3.6) and (3.7) the thickness of the sample, l , constitutes the main error for determining the optical properties of the material by THz TDS.¹⁷ By using the wrong sample thickness the resulting optical properties will oscillate as functions of frequency. Therefore, the best way of accurately determining the complex refractive index of the material is to simultaneously determine its effective thickness. We do this by measuring the oscillation amplitude for various thicknesses and correspondingly choose the thickness with the least oscillations as the correct thickness. An example is shown in Fig. 3.1, samples of different thicknesses have been attempted to fit eq. (2.56) with parameters $l = 50 \mu\text{m}$ and $\hat{n} = 3.42 + i0$. The oscillation amplitudes are lower for thicknesses closer to the real thickness.

For a thin sample, i.e. a sample which has a pulse width shorter than the optical thickness of the sample, the multiply reflected pulses are not easily separated, and the Fabry-Perot terms from eq. (2.56) must be included in the transfer function. Figure 3.2 shows two THz-pulses that have passed through a medium with no dispersion and no absorption, but for two different thicknesses of the medium. For the thick sample, the signal reduces to zero between the multiple reflections, which are easily distinguished. For the thin sample, the pulse seems broader than for the thick sample. The multiple reflections are so close to each other that they are indistinguishable. An iterative procedure is required to determine the optical parameters when

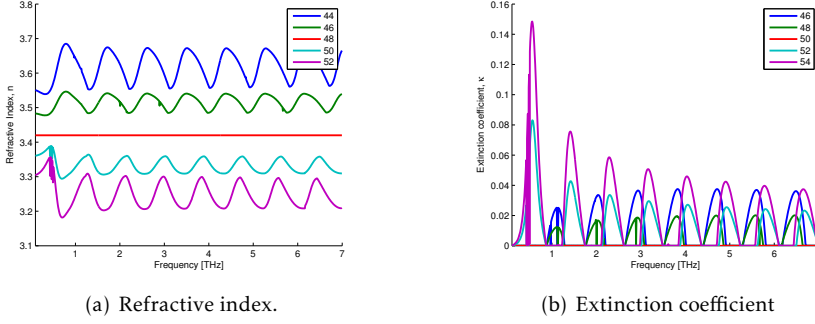


FIGURE 3.1: Optical parameters for various thicknesses (in microns).

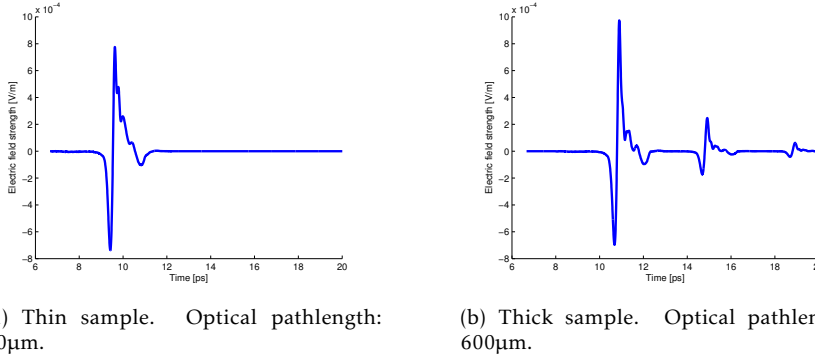


FIGURE 3.2: THz pulses that have passed through samples of different thickness

multiple reflections are included in the measurement.. Duvillaret *et al*^{14,17} were the first to develop such a procedure in 1996. Many improvements and variations have been suggested over the years.^{18–21} The core of the iterative procedure is to minimize the difference between the measured transfer function $H(\omega)$ and an analytical expression $\hat{H}(\omega)$. Since the transfer function is complex there is error in both the phase, $P(\omega)$, and the magnitude, $M(\omega)$.

$$P(\omega) = \angle \hat{H}(\omega) - \angle H(\omega), \quad (3.8)$$

$$M(\omega) = |\hat{H}(\omega)| - |H(\omega)|. \quad (3.9)$$

The error for any given frequency can be expressed as

$$\text{Error}(\omega) = |P(\omega)| + |M(\omega)|. \quad (3.10)$$

By minimizing the error by adjusting $n(\omega)$ and $\kappa(\omega)$ we find the analytical expression $\hat{H}(\omega)$ closest to the measured transfer function $H(\omega)$. From the measurements, the difference in arrival time for the highest magnitude of the reference pulse and the sample pulse, Δt , is found. Knowing the difference in arrival times, i.e. how much the pulse is delayed due to passing through the medium, an initial guess can be made of the refractive index of the medium,

$$n_{guess} = \frac{c_0 \Delta t}{l} + n_{air}, \quad (3.11)$$

where l is the assumed thickness. In addition we make an initial guess at the extinction coefficient from the relation between the maximum amplitude of the reference and sample spectra. It is assumed that the attenuation of the maximum of the THz pulse in the sample is given by the following relation²⁰

$$|E_{s,max}| = |E_{r,max}| \exp\left(-\frac{\omega}{c_0} \kappa(\omega) l\right), \quad (3.12)$$

so for every frequency, the algorithm starts looking for the correct value of $\kappa(\omega)$ near

$$\kappa_{guess} = -\frac{c_0}{l\omega} \log\left(\frac{|E_{s,max}|}{|E_{r,max}|}\right). \quad (3.13)$$

The length of the measurement in time decides the number of reflections included in the expression. If t_{max} is the time measured from the peak of the reference pulse until the end of the measurement, the number of reflections, δ , can be expressed as²⁰

$$\delta \leq \frac{t_{max} c_0}{2n_{guess}} - \frac{1}{2}. \quad (3.14)$$

In this thesis the Nelder-Mead Simplex method has been used to minimize the error, as suggested by Pupeza *et al.*²⁰ The Nelder-Mead algorithm is explained in appendix A. Many methods have been proposed to determine which thickness causes the least oscillations. The most common method is to calculate the Total Variation (TV) of degree one for a sample thickness, l , given by the equations^{18,20}

$$D(m) = |n(m-1) - n(m)| + |\kappa(m-1) - \kappa(m)| \quad (3.15)$$

$$TV(l) = \sum_{m \in BW} D(m). \quad (3.16)$$

The idea is to sum up the deviation between neighbouring values of the optical parameters within the bandwidth (BW). For extremely thin samples, the Fabry-Pérot period extends over several GHz, and thus the major contributions to the TV-values are noise and dielectric dispersion, and is therefore not accurate enough. As an alternative, Scheller *et al.*²¹ proposed to perform a Fourier transform on the optical parameters within the bandwidth of the measurements to determine the oscillation strength. The Fourier transformed values lie in a so-called *Quasi - Space* (QS) with units of time. The oscillation strength appears as a spike in QS. The discrete QS-values, QS_k are computed as

$$QS_k = \sum_{n=0}^{N-1} [y(\omega_n) e^{-i2\pi k n/N}], k = 0, 1, \dots, N-1, \quad (3.17)$$

where $y(\omega_n)$ represents an optical parameter and N is the amount of sampling points. It is usually advantageous to use the real part of the refractive index $n(\omega)$ as $y(\omega_n)$ since it is less sensitive to amplitude fluctuations. In Quasi-Space, the abscissa in units of time is $x_{QS} = 2\pi/\omega$. However, it is convenient to plot the QS-values against the normalized abscissa $L_{QS} = x_{QS}c_0/2$, which has a unit of distance. The maximum value within the range

$$L_{min} = \frac{c_0}{2n\Delta f}, \quad (3.18)$$

$$L_{max} = \frac{1}{df} \frac{c_0}{4n} = c_0 \frac{T_{max}}{4n}, \quad (3.19)$$

is an indicator for the oscillation strength. Here Δf is the bandwidth, df is the spectral resolution and T_{max} is the end of the time-window of the measurement. The maximum value manifests itself as a peak at the optical thickness of the sample. Equation (3.18) accounts for the distinguishability of the QS-peak from its neighbouring values and consequently for the condition of comprising at least one single period of oscillation within the spectral window. Equation (3.19) is equivalent to the Nyquist-Shannon sampling theorem and the occurrence of at least one Fabry-Pérot reflection in the time-domain of the measurement.²¹ The Quasi-Space values as a result of a Fourier transform of the refractive index shown in Fig. 3.1(a), are shown in Fig. 3.3. It is clear that the peaks are higher for the thicknesses where the oscillations have the largest amplitudes.

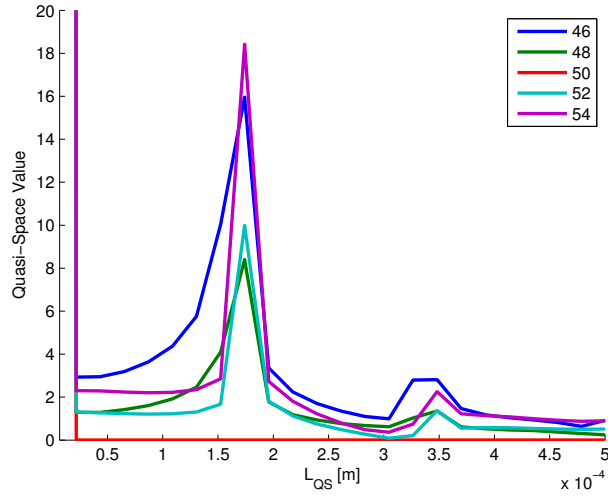


FIGURE 3.3: Quasi-Space values from the Fourier transform of $n(\omega)$ from Fig. 3.1(a). The peaks are located at $L_{QS} = 174 \mu\text{m}$, which is very close to optical thickness of the material $l_{opt} = n(\omega)l = 171 \mu\text{m}$.

Chapter 4

Simulation methods

This chapter describes the Finite Difference Time Domain (FDTD) algorithm, which can be used to simulate the propagation of an electromagnetic pulse passing through a medium. The FDTD method is able to simulate a pulse passing through a medium with either Lorentz- or Debye-permittivities.^a This allows us to watch how the pulse propagates through the different media. THz FDTD simulations have been found to be in good agreement with measurements of both layered structures²² and cancerous tissue.²³ This chapter offers a brief description of the algorithm based on 'Computational Electrodynamics - The Finite Difference Time Domain Method' by Allen Taflov²⁴ and 'Computational Electromagnetics' by Bondeson et al.²⁵

4.1 Finite Difference Time Domain algorithm

The **Finite-Difference Time-Domain** (FDTD) scheme is a numerical analysis technique used to find approximate solutions of a system of differential equations. From Maxwell's curl equations, eqs. (2.3) and (2.4) we see that the time-derivative of the E-field is dependent on the curl of the H-field (its spatial derivative). The time-derivative of the H-field and the spatial derivative of the E-field are related in a similar manner. The fields are offset temporally by half-steps in both the spatial and the temporal domain using the leap-frog technique (named after the children's game where you jump over one another). The E-field is updated at times $t = (n + 1/2)\Delta t$ and positions $x = l\Delta x$, while the H-field is updated at times $t = n\Delta t$ and positions $x = (l + 1/2)\Delta x$. With these half-steps we create a "Yee-grid". The discrete Maxwell equations become

$$\frac{H_y|_{l+1/2}^{n+1} - H_y|_{l+1/2}^n}{\Delta t} = \frac{1}{\mu_{l+1/2}} \left[\frac{E_z|_{l+1}^{n+1/2} - E_z|_l^{n+1/2}}{\Delta x} - \sigma^*|_{l+1/2} H_y|_{l+1/2}^{n+1/2} \right], \quad (4.1)$$

^aThe source material for this chapter is written in a different convention than the rest of this thesis. As a result, the expression for the Lorentz and Debye media, eqs. (2.25) and (2.41), are expressed with a positive term, $+i\omega t$, instead of $-i\omega t$, in the denominator. See appendix C for further explanation

$$\frac{E_z|_l^{n+1/2} - E_z|_l^{n-1/2}}{\Delta t} = \frac{1}{\epsilon_l} \left[\frac{H_y|_{l+1/2}^n - H_y|_{l-1/2}^n}{\Delta x} - \sigma_l E_z|_l^n \right]. \quad (4.2)$$

After a bit of work these are simplified to

$$H_y|_{l+1/2}^{n+1} = M_{l+1/2} H_y|_{l+1/2}^n + N_{l+1/2} \frac{E_z|_{l+1}^{n+1/2} - E_z|_l^{n+1/2}}{\Delta x}, \quad (4.3)$$

$$E_z|_l^{n+1/2} = O_l E_z|_l^{n-1/2} + P_l \left[\frac{H_y|_{l+1/2}^n - H_y|_{l-1/2}^n}{\Delta x} - J_{source_z}|_l^n \right], \quad (4.4)$$

where

$$M_{l+1/2} = \frac{2\mu_{l+1/2} - \sigma_{l+1/2}^* \Delta t}{2\mu_{l+1/2} + \sigma_{l+1/2}^* \Delta t}, \quad (4.5)$$

$$N_{l+1/2} = \frac{2\Delta t}{2\mu_{l+1/2} + \sigma_{l+1/2}^* \Delta t}, \quad (4.6)$$

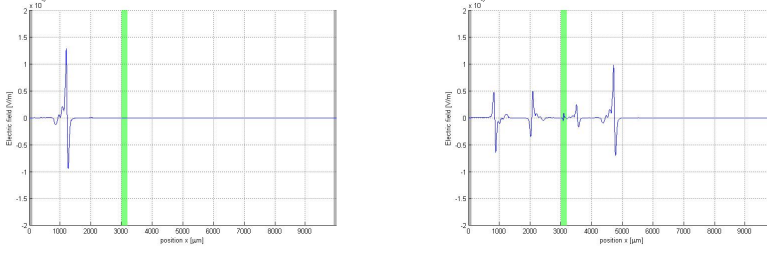
$$O_l = \frac{2\epsilon_l - \sigma_l \Delta t}{2\epsilon_l + \sigma_l \Delta t}, \quad (4.7)$$

$$P_l = \frac{2\Delta t}{2\epsilon_l + \sigma_l \Delta t}. \quad (4.8)$$

The step size is limited by the condition $c\Delta t/\Delta x = R \leq 1$. If $R = 1$ the dispersion caused by numerical accuracy is at its minimum. The terms σ and σ^* are the electric and magnetic conductivities, respectively. They are zero anywhere but the edges of the spatial grid. There they are set so that

$$\frac{\sigma^*}{\mu_0} = \frac{\sigma}{\epsilon_0}, \quad (4.9)$$

at the boundaries so that they act as an absorbing outer layer to the grid. The "future" fields are expressed in terms of "past" fields. The trick now is to update the electric field one time-step into the future. Then this "future" field essentially becomes a known "past" field. Then we use this field to update and find the future magnetic field, which can be used to find the next future electric field, and so on. Section 4.1 shows a THz pulse before and after it comes in contact with a 200 μm thick sample with no dispersion and no absorption. The smaller pulses that have been reflected back and forth within the medium and refracted at both interfaces can be seen. Figure 4.1(b) essentially shows the same scenario as Fig. 2.4, but for normal incidence.



(a) A THz pulse propagating towards a 200 μm thick sample.

(b) Multiple reflections.

FIGURE 4.1: A THz pulse passing through a sample without any dispersion or absorption, causing multiple reflections. The green area is the sample. The left and right boundaries are absorbing layers.

4.2 Dispersion

In section 2.2 the resonant Lorentz and Debye media were introduced. In order to simulate these, the auxiliary differential equation method is implemented. Instead of updating the E and H field in the standard FDTD, the displacement field D is calculated and coupled with the magnetic field, H . The absorptive and dispersive behaviour is handled in a supplementary equation for the E -field.,

$$H_y|_{l+1/2}^{n+1} = M_{l+1/2} H_y|_{l+1/2}^n + N_{l+1/2} \frac{E_z|_{l+1}^{n+1/2} - E_z|_l^{n+1/2}}{\Delta x} \quad (4.10)$$

$$D_z|_l^{n+1/2} = O'_l D_z|_l^{n-1/2} + P'_l \left[\frac{H_y|_{l+1/2}^n - H_y|_{l-1/2}^n}{\Delta x} - J_{source_z}|_l^n \right] \quad (4.11)$$

$$E_z|_l^{n+1/2} = f(D^{n+1/2}, D^{n-1/2}, D^{n-3/2}, \dots, E^{n-1/2}, E^{n-3/2}, \dots) \quad (4.12)$$

where

$$O'_l = \frac{2 - \sigma_l \Delta t}{2 + \sigma_l \Delta t} \quad (4.13)$$

$$P'_l = \frac{2 \Delta t}{2 + \sigma_l \Delta t} \quad (4.14)$$

If we know the analytic solution of the permittivity, $\epsilon(\omega)$, we can use the relation between the E and D fields,

$$\epsilon(\omega) = \epsilon_0 \epsilon_r(\omega) = \frac{D(\omega)}{E(\omega)}, \quad (4.15)$$

and perform an inverse Fourier transform to find an ordinary differential equation. The inverse Fourier transform of the frequency terms correspond to temporal derivatives,

$$(i\omega)^n \Rightarrow \frac{\partial^n}{\partial t^n}. \quad (4.16)$$

4.2.1 Debye medium

By inserting the expression for the Debye medium, eq. (2.41), into eq. (4.15)^b we obtain the following expression,

$$\epsilon_0 \epsilon_\infty (1 + i\omega\tau) E(\omega) + \epsilon_0 (\epsilon_s - \epsilon_\infty) E(\omega) = (1 + i\omega\tau) D(\omega). \quad (4.17)$$

Through a Fourier transform we find

$$\epsilon_0 \epsilon_s E(t) + \epsilon_0 \epsilon_\infty \tau \frac{\partial E(t)}{\partial t} E(t) = D(t) + \tau \frac{\partial D(t)}{\partial t}. \quad (4.18)$$

The finite difference scheme is applied to this equation, and to ensure stability, we take the averages of the current-time values.

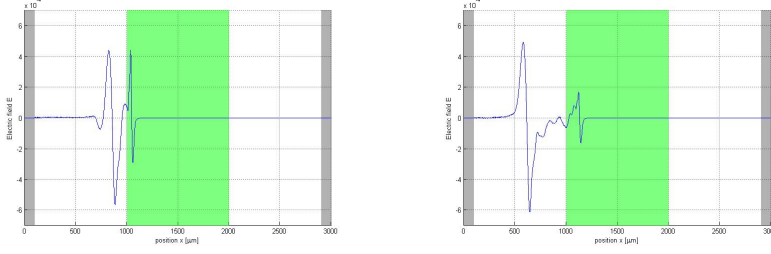
$$E^n \Rightarrow \frac{E^{n+1} + E^n}{2}. \quad (4.19)$$

The result is

$$E^{n+1} = D^{n+1} \frac{\frac{1}{2} + \frac{\tau}{\Delta t}}{\epsilon_0 (\frac{\epsilon_s}{2} + \epsilon_\infty \frac{\tau}{\Delta t})} + D^n \frac{\frac{1}{2} - \frac{\tau}{\Delta t}}{\epsilon_0 (\frac{\epsilon_s}{2} + \epsilon_\infty \frac{\tau}{\Delta t})} - E^n \frac{\frac{\epsilon_s}{2} - \epsilon_\infty \frac{\tau}{\Delta t}}{\frac{\epsilon_s}{2} + \epsilon_\infty \frac{\tau}{\Delta t}}. \quad (4.20)$$

This expression takes the role of eq. (4.12). Section 4.2.1 shows a THz pulse entering a Debye medium. The pulse is absorbed as it passes through the medium. This figure illustrates why it we want to measure thin samples. The sample shown in the figure is very thick (1 mm), so the amount of THz exiting the medium on the backside is so small that nothing can be learned from it except for the qualitative knowledge that the medium absorbs the THz. Even this is not necessarily true as the THz might not even have entered into the medium, but been reflected of the surface.

^bNote the sign change in the denominator



(a) The THz pulse shortly after it enters the medium.

(b) Absorption.

FIGURE 4.2: A THz pulse passing through a Debye medium. This sample is much, much longer than the pulse width, so it can easily be classified as a thick medium.

4.2.2 Lorentz medium

For a Lorentz medium the insertion of eq. (2.26) into eq. (4.15) yields^c

$$\epsilon_0[\epsilon_s\omega_0^2 + \epsilon_\infty(i\omega\gamma - \omega^2)]E(\omega) = [\omega_0^2 - \omega^2 + i\gamma\omega]D(\omega). \quad (4.21)$$

Since $-\omega^2 = (i\omega)^2$, the Fourier transform yields,

$$\epsilon_0\left[\epsilon_s\omega_0^2 + \epsilon_\infty\left(\gamma\frac{\partial}{\partial t} + \frac{\partial^2}{\partial t^2}\right)\right]E(t) = \left[\omega_0^2 - \gamma\frac{\partial}{\partial t} + \frac{\partial^2}{\partial t^2}\right]D(t). \quad (4.22)$$

By applying the second-order central-difference scheme centered on time-step n , where

$$\frac{\partial^2 E^n}{\partial t^2} = \frac{E^{n+1} - 2E^n + E^{n-1}}{(\Delta t)^2}, \quad (4.23)$$

$$\frac{\partial E^n}{\partial t} = \frac{E^{n+1} - E^{n-1}}{2\Delta t}, \quad (4.24)$$

$$E^n = \frac{E^{n+1} + E^{n-1}}{2}, \quad (4.25)$$

^cIn the literature, this is referred to as a "Second-Order Lorentz medium". This does not mean that the permittivity $\epsilon_r(\omega)$ is of a higher complexity than eq. (2.26). See for example eq. (2.44). The reason for naming it "Second-Order" is that it includes second-derivatives in the time domain, see eq. (4.22). Since the Debye medium only includes the first derivative of D and E it is referred to as the "First-Order Debye medium".

the following expression is obtained

$$\begin{aligned} & \epsilon_0 E^{n+1} \left(\frac{\epsilon_\infty}{(\Delta t)^2} + \frac{\omega_0^2 \epsilon_s}{2} + \frac{\epsilon_\infty \gamma}{2\Delta t} \right) - 2E^n \frac{\epsilon_\infty}{(\Delta t)^2} + \epsilon_0 E^{n-1} \left(\frac{\epsilon_\infty}{(\Delta t)^2} + \frac{\omega_0^2 \epsilon_s}{2} - \frac{\epsilon_\infty \gamma}{2\Delta t} \right) \\ &= D^{n+1} \left(\frac{1}{(\Delta t)^2} + \frac{\omega_0^2}{2} + \frac{\gamma}{2\Delta t} \right) - \frac{2D^n}{(\Delta t)^2} + D^{n-1} \left(\frac{1}{(\Delta t)^2} + \frac{\omega_0^2}{2} - \frac{\gamma}{2\Delta t} \right). \end{aligned} \quad (4.26)$$

The expression for E^{n+1} becomes

$$\begin{aligned} E^{n+1} &= \frac{1}{\epsilon_0 \left(2\epsilon_\infty + \epsilon_\infty \gamma \Delta t + \epsilon_s (\omega_0 \Delta t)^2 \right)} \times \\ & \left[D^{n+1} \left(2 + \gamma \Delta t + (\omega_0 \Delta t)^2 \right) - 4D^n + D^{n-1} \left(2 - \gamma \Delta t + (\omega_0 \Delta t)^2 \right) \right. \\ & \left. + \epsilon_0 E^{n-1} \left(2\epsilon_\infty - \epsilon_\infty \gamma \Delta t + \epsilon_s (\omega_0 \Delta t)^2 \right) - 4E^n \epsilon_0 \epsilon_\infty \right]. \end{aligned} \quad (4.27)$$

The simulation of the Lorentz medium shows essentially the same scenario as section 4.2.1.

Now that we have studied both dull and interesting media, through both theory and simulations, we are well equipped in our understanding of any type of media and how they interact with electromagnetic pulses.

Chapter 5

Experimental methods

In this chapter, the experimental setup used for the measurements presented in this thesis, is described. Some unknowns and assumptions concerning the measurements are discussed.

5.1 Experimental setup

An infrared (IR), femtosecond (fs) laser pulse with wavelength close to 800 nm is split in two parts, a pump and a probe. The probe pulse passes through a variable delay line. By varying the delay line of the probe-beam, we can measure the temporal shape of the THz-pulse by measuring the probe beam, which polarization at a specific time has been altered by the THz pulse present in the electro-optic crystal at the same time.

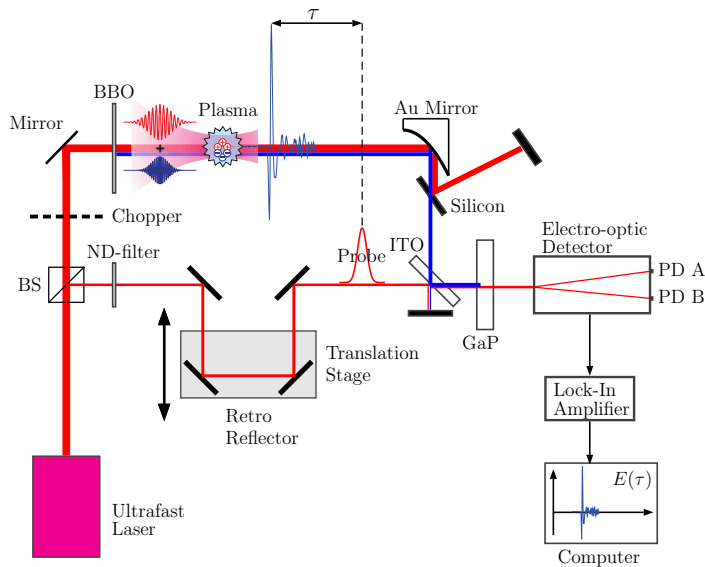


FIGURE 5.1: Experimental setup.

The pump-pulse is chopped by a chopper at 200 Hz and passes through a BBO crystal, generating a second harmonic signal. The initial pulse and the second harmonic are focused by a lens and interact in a plasma creating the THz pulse, as explained in section 2.4.3. The polarization of the generated THz pulse is unknown. The THz and the IR are focused by an off-axis parabolic mirror, which collimates the beam. The beam then passes through a silicon wafer that is angled so that it is close to the Brewster angle for THz. Most of the IR beam is reflected by the Si, and does not interfere with the measurement. Having the Silicon wafer at the Brewster angle will change the polarization of the THz so that it is linearly polarized.²⁶

After the THz has passed through the silicon wafer, it passes through the material sample. The beam diameter at the focus is 1 mm. Elsewhere, it is 1 cm. The sample is not shown in Fig. 5.1, but it would be placed between the silicon and the ITO. Thereafter, the THz and the probe beam are combined by a glass substrate coated with a thin layer of tin doped Indium Oxide (ITO). The ITO lets almost all optical frequencies pass through (up to 95%), but reflects almost all of the THz (up to 98%). The beams are then pass into a Gallium Phosphide (GaP) crystal, causing the THz electric field to change the polarization of the IR-beam, which is subsequently detected by the photo-detector. A schematic overview of the setup is shown in Fig. 5.1. Part of the system, from the BBO to the GaP, is contained within a box which is pumped with dry air. This is to reduce the amount of water vapor present, which reacts very strongly to THz radiation. An measured THz pulse is shown in Fig. 5.2. The smaller pulses are multiple reflections from the electro-optic GaP crystal, which acts as a Fabry-Pérot etalon. The pulse shown in the figure is the average value for ten consecutive measurements.

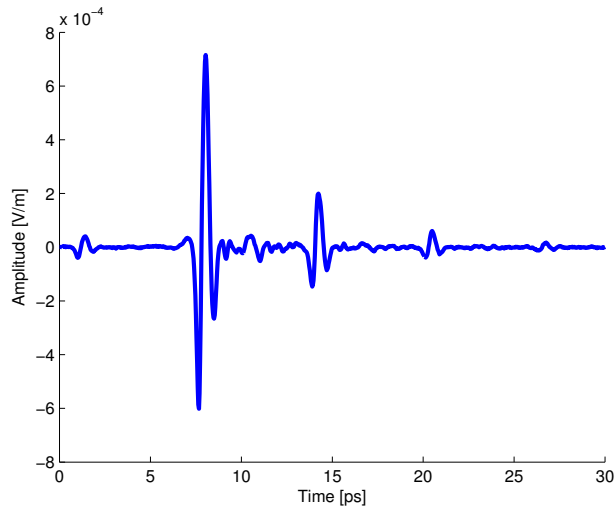


FIGURE 5.2: An example of a measured THz pulse. The smaller pulses are reflections from the GaP crystal.

5.2 Assumptions and uncertainties

When measuring samples with THz-TDS, some assumptions have to be made. It is assumed that:¹⁴

1. The sample is homogenous, with two flat and parallel sides
2. The sample is magnetically isotropic without surface charges
3. That scattering off the sample is negligible
4. The sample has a linear electromagnetic response
5. The pulse is a plane wave and has normal incidence upon the sample
6. The pulse is linearly polarized, parallel to the optical axis of the detector
7. That the measurements are performed in a dry atmosphere

The assumptions made concerning the sample and the pulse being a plane wave are necessary for the validity of the model used for the interaction between the THz pulse and the sample. If the incidence is close to normal

the effect of a small angle variation is negligible.²⁰ This can easily be seen from the cosine-terms in eqs. (2.52) and (2.53) when normal incidence means that the incidence angle $\theta_i \approx 0$, so that $\cos \theta_i \approx 1$. The measurements are performed within a closed box that has been pumped with dry air. However, since we had no equipment for measuring the humidity inside the box, the difference in humidity between the sample- and the reference measurements might affect the measurements. In addition, there are a few random and systematic factors that could affect the measurements. Random errors are^{17,27}

1. Electronic background noise of the detector
2. Intensity fluctuations of the pump-laser
3. Jitter in the variable delay line of the probe beam.

The first two factors are random noise from the system itself. Performing several measurements and calculating the mean values will reduce their influence since they are random fluctuations. The drift in the pump-laser may cause the intensity of the pulse to vary. Performing shorter measurements, or increasing the step-length of the variable delay line could reduce the amount of drift over the course of the measurement. However, measuring over a shorter time will reduce the resolution in Fourier space. Increasing the step-length of the delay-line could affect the determination of the delay between the sample and the reference pulse. Systematic errors could include

1. Registration errors.
2. Mechanical drift
3. Multiple reflections within plane parallel optical components

For very thin samples, these errors can become relatively strong. In the worst case, the systematic error that progresses linearly over time may be misinterpreted as the presence of a sample.²⁸

5.2.1 Signal to noise ratio and dynamic range

The quality of data is conventionally communicated by giving the Signal to Noise Ratio (SNR) and Dynamic Range (DR) of the measurements. Signal to noise ratio is exactly what it sounds like, the ratio between the level of the desired signal and the level of the background noise. Dynamic Range is the ratio between the highest and lowest values of the measurements. In a

system where amplitude is measured, such as we do in THz-TDS, SNR and DR are defined as

$$SNR = \frac{\text{mean magnitude of amplitude}}{\text{standard deviation of amplitude}}, \quad (5.1)$$

$$DR = \frac{\text{maximum magnitude of amplitude}}{\text{rms of noise floor}}. \quad (5.2)$$

The recommended procedure used for calculating DR and SNR is as follows²⁹

1. Measure the time-domain trace and note the value of the peak maximum.
2. Measure the noise signal in the absence of THz, e.g., before the arrival of the main pulse.
3. The mean signal in the absence of THz should be constant (zero for electro-optic detection, nonzero for a photoconductive antenna). Calculate its standard deviation.
4. DR = mean magnitude of the peak/standard deviation of noise.
5. SNR=mean magnitude of the peak/standard deviation of the peak.

There are ways of performing this calculations in the frequency-domain, but in this thesis we will perform the calculation in the time-domain. The Dynamic Range of the measurement determines the largest detectable absorption coefficient.

$$\alpha_{max}d = 2\ln\left(DR \frac{4n}{(n+1)^2}\right). \quad (5.3)$$

This corresponds to the sample signal being attenuated to the level of the noise floor. In other words, if the absorption is so strong that the signal would be brought beneath the noise level, i.e. $\alpha > \alpha_{max}$, the analysis will show an apparent absorption coefficient equal to α_{max} .³⁰ This stresses the importance of measuring samples that are thin enough so the THz pulse can pass through without being attenuated to the level of the noise floor. The highest dynamic range for the measurements presented in this thesis was ≈ 1900 . The measurements presented in this thesis were performed on samples with low absorption so this does not come in to play in the analysis of the data presented later on in chapter 6.

Chapter 6

Results

The optical parameters of silicon in the THz regime have been extensively studied and are well documented. By testing samples of varying thickness it can be determined if there are any limitations to either the minimization method or the determination of the correct thickness. In the beginning of this chapter, the results of the measurements of several thin layers of silicon are presented. Later, the minimization method is applied to the results of the FDTD simulation. By doing so it can be determined whether or not the FDTD simulation gives an accurate image of the real situation. Furthermore, it allows for testing of the minimization and the thickness-determination method on more complicated materials through simulations of resonant Lorentz- and Debye media.

6.1 Measurements

In this section the calculated optical parameters of different samples are presented. Silicon samples of different thickness were measured. The optical parameters of silicon are well documented to be $\hat{n} = 3.42 + i0$.^{14,17,18,20,21} From the results we will attempt to answer the following questions: Does the error-minimization method work for a noisy transfer function, and are we able to find a thickness for which the oscillating behaviour of the optical parameters are at a minimum? Are the results as expected? Are the measurements affected by the additional Fabry-Pérot reflections from the electro-optic crystal?²⁷ This would limit the frequency resolution of the spectra by limiting the measurements time-window. Lastly, we want to determine if there are thicknesses for which we are unable to find the correct thickness with either the Quasi-Space method, or with total variation.

6.1.1 50 micron silicon sample

Figure 6.1 shows two THz pulses in time (in picoseconds, ps), vertically offset for clarity. The peaks appearing close to 4 ps are the main peaks, while the peaks appearing close to 10 ps are reflections caused by the Fabry-Pérot effect from the electro-optic (EO) crystal used in the experimental setup.

The time window can be modified to exclude these reflections. The sample pulse arrives later than the reference pulse and the amplitude is much lower. A reflected pulse from the sample can be seen at around 6 ps. Figures 6.2(a) and 6.2(b) shows the Fourier spectra of the pulses with and without the reflections from the EO-crystal. When the reflections from the crystal are removed, one can clearly see the oscillations that are expected from a Fabry-Perot. When the reflections are included the Fourier spectra includes the oscillations from both the sample and the crystal, which makes the spectrum appear very noisy. The signal strength of the reference spectrum falls sharply down to the noise-floor at around 7 THz. Figure 6.3 shows the transfer function calculated for the two cases, where the graph labeled "short" is for the limited time window excluding the reflections from the EO-crystal. The two transfer functions are not exactly identical, but there isn't any consequent difference as one would expect from the periodic Fabry-Pérot oscillations. Depending on the input for the minimization, the long and the short measurements may or may not select the same thickness. Figure 6.4 shows the values of the Quasi-Space peaks and the Total Variation the measurement for thicknesses between 58 and 70 microns with a step length of 0.1 micron. Both the Quasi-space values for the Fourier transform of $n(\omega)$ and the Total variation finds a minima at $64.3 \mu\text{m}$ for the long measurement. For the short measurement, the minima are both found at $64.8 \mu\text{m}$, but there is very little difference in the calculated optical parameters.

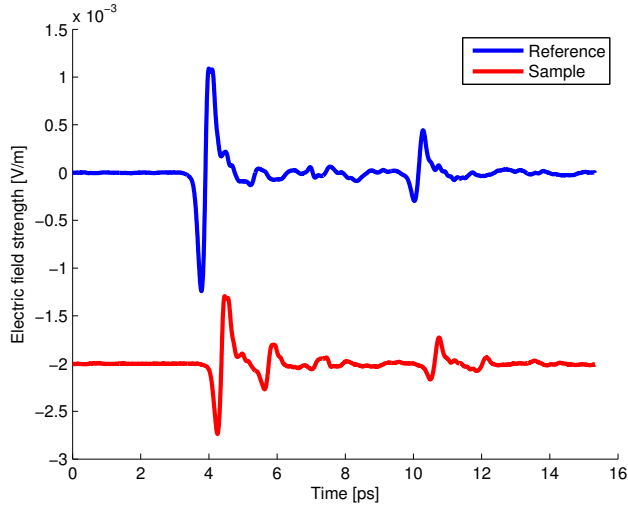
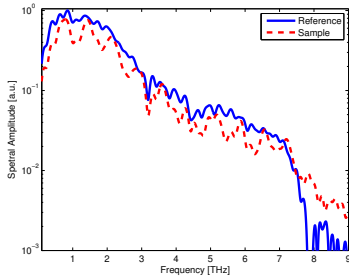
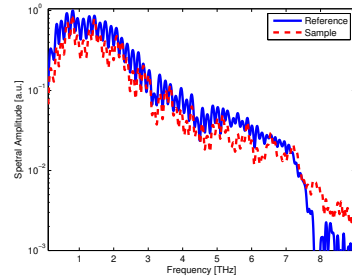


FIGURE 6.1: Reference pulse and sample pulse from a 64.3 micron thick silicon wafer, vertically offset for clarity.



(a) Without Fabry-Pérot reflections from the crystal



(b) Including Fabry-Pérot reflections from the crystal.

FIGURE 6.2: Fourier spectra of the reference and the sample pulses with and without the extra reflections from the electro-optic crystal.

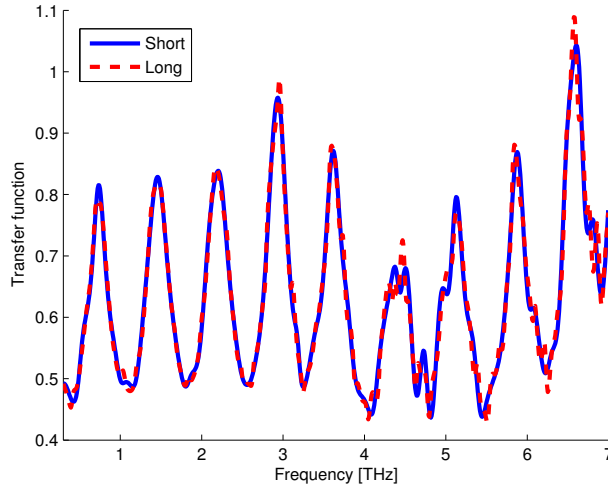
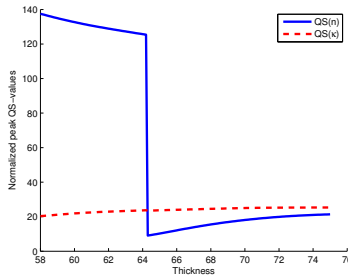
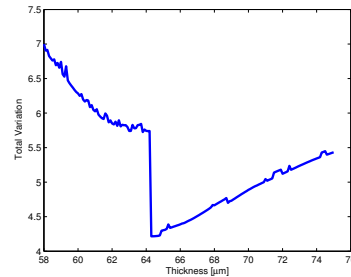


FIGURE 6.3: Transfer function for with and without the additional reflections from the electro-optic crystal.

Figures 6.5(a) and 6.5(b) shows the resulting optical parameters, n and κ for the determined thickness, $64.3 \mu\text{m}$. Neither of the values are as expected. Figure 6.6 shows the transfer function obtained by the measurement and the



(a) Quasi-Space values



(b) Total variation.

FIGURE 6.4: Measure of oscillations in the optical parameters for different thicknesses

transfer function found by the minimalization of the error. The algorithm is limited by $\kappa \geq 0$ so the maximum value of the numerical transfer function is 1. The transfer function and the optical parameters are calculated within the bandwidth $0.3 - 7 \text{ THz}$.

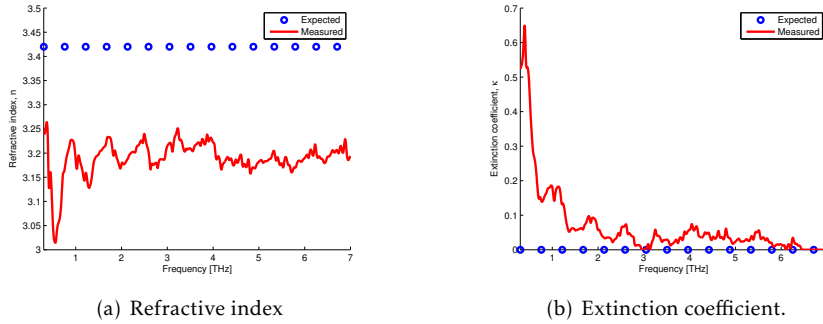


FIGURE 6.5: Optical parameters for measurement of an allegedly 50 μ m thick silicon wafer. The expected value is $\hat{n} = 3.42 + i0$.

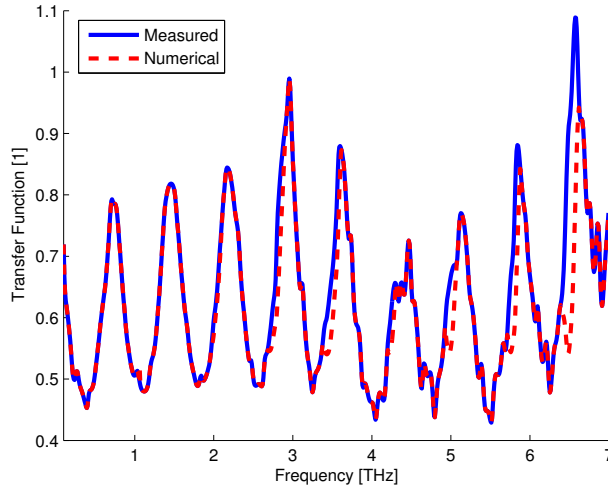


FIGURE 6.6: Measured transfer function as well as the transfer function found through numerical approximation.

6.1.2 10 micron silicon sample

Figure 6.7 shows the Quasi-Space values and the total variation for thicknesses 8 – 14 μ m with a step-length of 0.1 μ m. The Quasi-Space method finds a minimum at 11.3 μ m, while the total variation fails to determine a minimum. Figure 6.8 shows the optical parameters at the chosen thickness.

There are very clear oscillations in both parameters. Figure 6.9 shows the

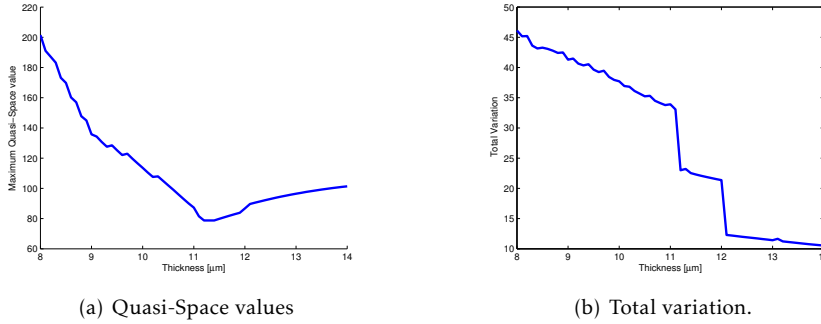


FIGURE 6.7: Measure of oscillations in the optical parameters for different thicknesses

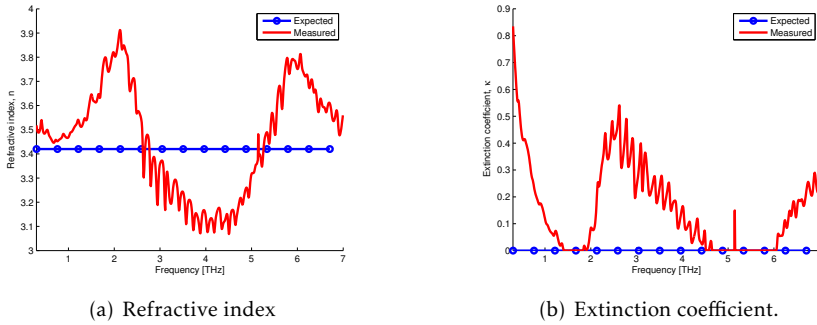
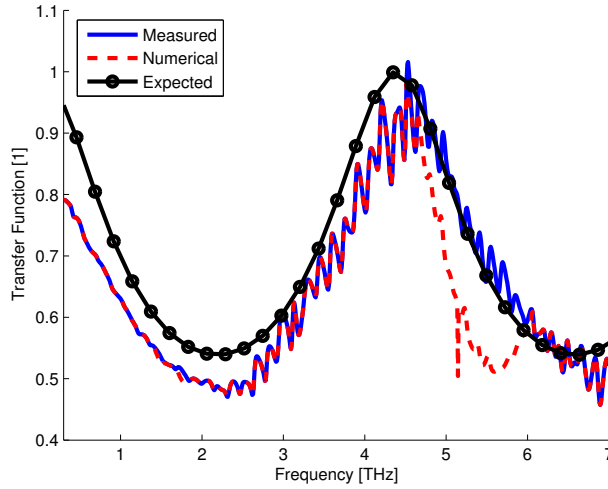


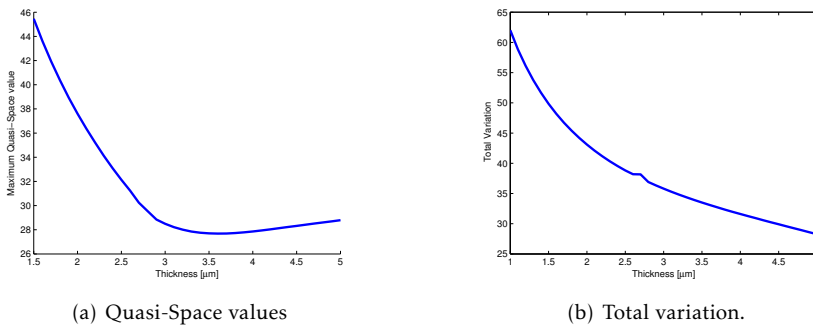
FIGURE 6.8: Optical parameters for measurement of an allegedly 10μm thick silicon wafer. The expected value is $\hat{n} = 3.42 + i0$. The mean value of the refractive index is 3.46

measured transfer function and the numerical fit for the chosen thickness of 11.3 μm with the expected transfer function for a 10 μm silicon sample. The numerical fit deviates from the measurement between 4.5 and 6 THz.

FIGURE 6.9: Transfer function for the 10 μm silicon sample.

6.1.3 2 micron silicon sample

The thickness of the 2 μm sample was determined by the Quasi-Space values of $n(\omega)$ to be 3.6 microns thick. The total variation does not manage to find a minimum. Both are shown in Fig. 6.10 The calculated optical parameters are shown in Fig. 6.11. Figure 6.12 shows that the measured and expected transfer functions are very different.

FIGURE 6.10: Quasi-Space values and total variation for the measurements of the 2 μm sample.

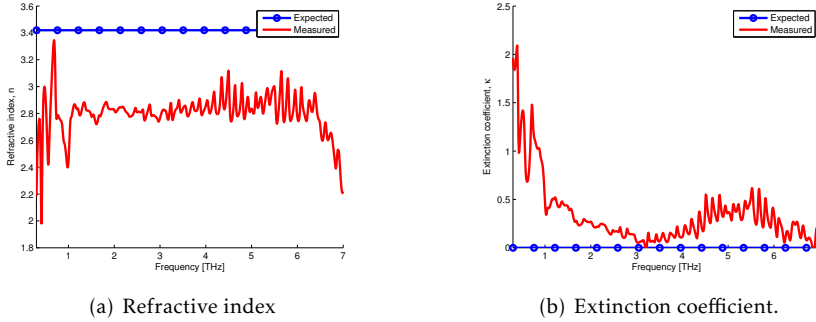


FIGURE 6.11: Optical parameters for measurement of a 2 micron thick silicon wafer. The expected value is $\hat{n} = 3.42 + i0$.

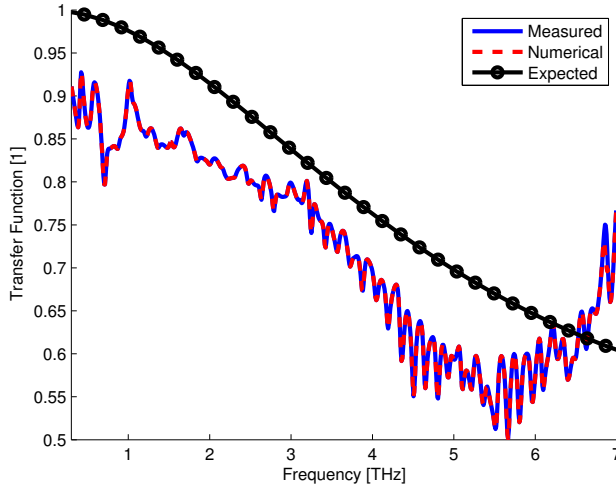


FIGURE 6.12: Transfer function for the 2 μm silicon sample.

Now that the algorithm for parameter determination has been tested for a dispersionless sample, it is time to test it for more interesting media. Due to problems with the equipment, measurements of samples with resonances were not conducted. Instead, the algorithm is tested on samples simulated by a FDTD simulation.

6.2 Simulations

In this section the results of the FDTD simulations are presented. We begin with extracting the optical parameters from a simulation of a non-absorptive, non-dispersive material to see if the FDTD simulation has any merit. Later on, we attempt to extract the parameters from more complex materials modeled in the form of Lorentz- and Debye media.

An actual, measured THz pulse was used as an input in the FDTD simulation where the pulse propagates through samples of various thicknesses and permittivities. The temporal time-step of the measurement was $\Delta t = 6.6666$ femtoseconds. The corresponding spatial time-step was $\Delta x = \Delta t/c \approx 2 \mu\text{m}$. Figure 6.13(a) shows the transfer function obtained by the simulation for a $50 \mu\text{m}$ thick sample with refractive index $\hat{n} = 3 + i0$. There is a very clear difference, which increases with frequency. To increase the precision of the simulation, the measured pulse was interpolated with a factor 2 so that the temporal step length became 3.33 fs and the spatial step length became $1 \mu\text{m}$. This reduced the difference between the simulation and the theoretical expressions considerably. The transfer function with the improved precision is shown in Fig. 6.13(b). Attempts at further interpolations did not result in a successful simulation. For a number of simulations, the thicknesses found

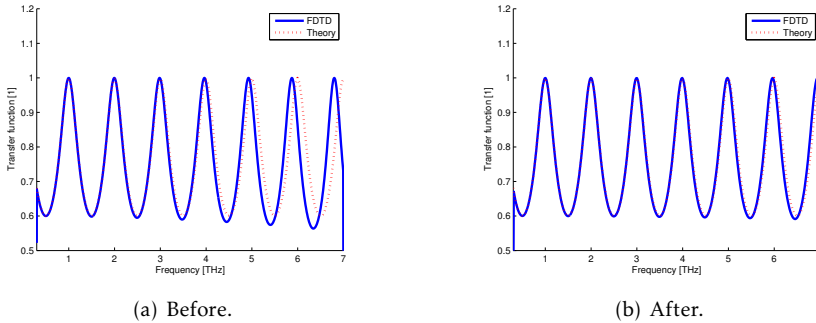


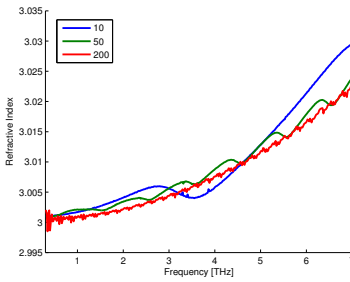
FIGURE 6.13: Transfer function of a simulated non-dispersive, non-absorbing material with thickness $50\mu\text{m}$ and refractive index $n = 3$. The two figures shows the simulation before and after the input pulse has been interpolated.

by the Fourier transform of the different optical parameters within $\pm 2 \mu\text{m}$ of the assumed values, are listed in table 6.1. Figures 6.14(a) and 6.14(b) shows the optical parameters extracted from simulations through samples of thickness 10, 50 and $200 \mu\text{m}$.

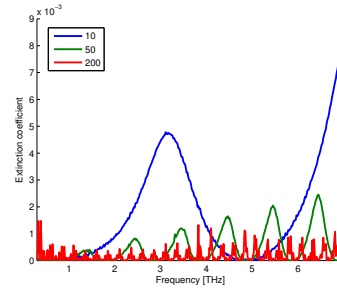
TABLE 6.1: Simulation thickness and thicknesses found by the Fourier transform of the different optical parameters.

Simulation input [μm]	n [μm]	κ [μm]	TV
2	2.2	2.7	0.6
4	3.9	3.7	3.9
6	6.0	5.7	5.9
8	8.0	7.9	7.9
10	10.1	10.0	9.9
50	50.3	50	50
200	199	200.1	200

Both the Quasi-Space method and the total variation method seems to work well in indicating what the correct thickness is, but it becomes more difficult as the thickness is reduced.



(a) Refractive index for FDTD simulation for various thicknesses. Input: $n = 3$.



(b) Extinction coefficient for FDTD simulation for various thicknesses. Input: $\kappa = 0$.

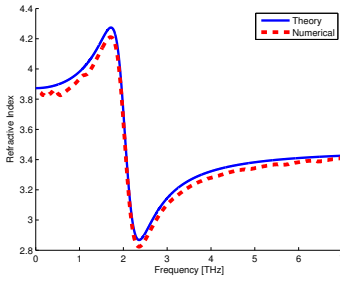
FIGURE 6.14: Calculated optical parameters for simulations of various thicknesses of a non-absorbing and non-dispersive medium.

From the table 6.1 and Figs. 6.14(a) and 6.14(b) it seems as the largest error in the simulation lies in the fact that the computed medium is dispersive. If the relation $c\Delta t/\Delta x \neq 1$, there will be a non-linear dispersion relation. Decreasing the temporal and spatial time-steps by interpolating the pulse clearly increases the precision. There is some absorption, which seems to increase as the thickness decreases. A possible cause for the error in the simulation is the fact that due to the reflections between the sample surfaces become more frequent for thinner samples, more calculations must be made, probably causing some small errors. In Fig. 6.14 it is clear that both $n(\omega)$

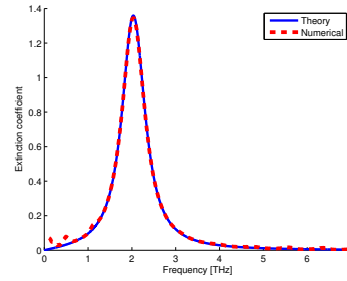
and $\kappa(\omega)$ are oscillating, with a longer period for a shorter medium. This behaviour is analogous to that of a Fabry-Pérot etalon.

6.2.1 Lorentz medium

The optical parameters of an imagined Lorentz medium with parameters $\epsilon_s = 15$, $\epsilon_\infty = 12$, $\omega_0 = 2$ THz, $\gamma = 0.3\omega_0$ and thickness $50\text{ }\mu\text{m}$ are shown in Fig. 6.15. The Total Variation method manages to find a minimum at $51.9\text{ }\mu\text{m}$. Both the parameters and the transfer function found at this thickness fit better with the theoretical values than those found at $50\text{ }\mu\text{m}$. The spectrum of the simulated pulse, the transfer function, as well as its numerical fit are shown in Fig. 6.16. Both the absorption peak and the oscillating behaviour caused by the Fabry-Pérot effect are apparent.

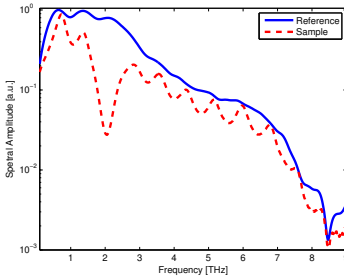


(a) Refractive index

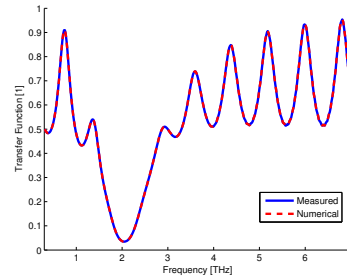


(b) Extinction coefficient.

FIGURE 6.15: Theoretical and numerical optical parameters for a Lorentz medium.



(a) Spectrum



(b) Transfer function

FIGURE 6.16: Spectrum and transfer function for the simulated Lorentz medium

6.2.2 Debye medium

The optical parameters of an imagined Debye medium with parameters $\epsilon_s = 15$, $\epsilon_\infty = 8$, $\tau = 0.4$ ps and thickness $50 \mu\text{m}$ are shown in Fig. 6.17. The Total Variation method manages to find a minimum at $51.5 \mu\text{m}$. The spectrum of the simulated pulse and the transfer function and its numerical fit are shown in Fig. 6.18.

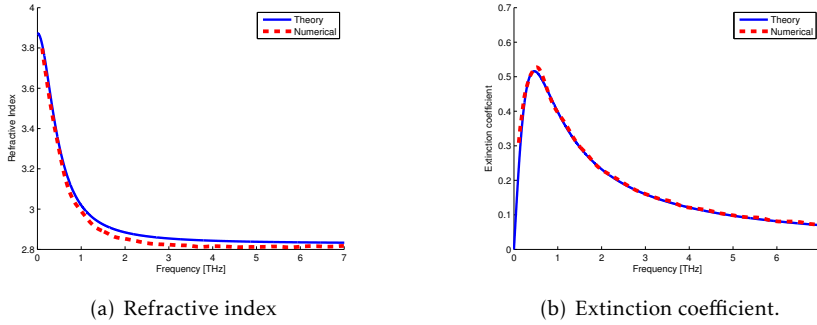


FIGURE 6.17: Theoretical and numerical optical parameters for a Debye medium.

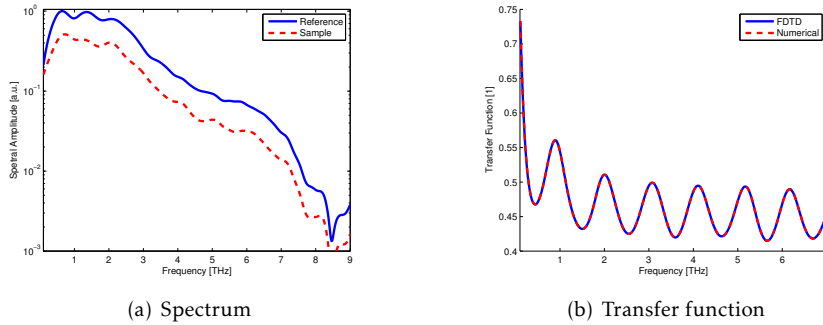


FIGURE 6.18: Spectrum and transfer function for the simulated Debye medium

Chapter 7

Discussion

In this chapter, we discuss the measurements and the simulation, what sorts of errors are present, and how they affect the error minimization method and the choice of the correct thickness.

7.1 Errors in the minimization method

The method of minimizing the error between the measured and theoretical transfer functions was first tested by letting it attempt to minimize a theoretical transfer function, following eq. (2.58). The MATLAB function 'fminsearch' employs the Nelder-Mead simplex method to minimize the error. The imagined sample had a thickness of $l = 50 \mu\text{m}$ and had a refractive index $\hat{n} = 3.42 + i0$, which is the refractive index of silicon, the same as was presented in Fig. 3.1. The assumed time difference between the arrival of the reference pulse and the sample pulse was simply set to $\Delta t = l(n_{sam} - n_{air})/c_0$. The initial guess-values for $n(\omega)$ and $\kappa(\omega)$ were calculated from eqs. (3.11) and (3.13). In Fig. 7.1(b) one can clearly see that, for the real part, $n(\omega)$, that there are some anomalies from an otherwise sinusoidal shape. These spikes cannot be explained from the theory in section 2.2, so it can be assumed that these values are invalid. The assumed cause for these spikes is that the minimization algorithm fails to converge towards the correct minimum. Since this test was performed on an analytical expression for the transfer function, it is apparently not a product of measurement noise. Figure 7.1(b) shows the result of the Fourier transform of the refractive index into Quasi-Space. The peaks are a lot less distinct than what we saw earlier in Fig. 3.1. This increase in the Quasi-Space values could affect the choice of thickness. The spikes in the refractive index could be removed before the Fourier transform is made in order to better determine the Quasi-Space values. For a non-dispersive, non-absorbing sample the spikes could be removed simply by removing any values outside a few standard deviations from the mean values, but this is not necessarily a valid option for other types of media where the refractive index isn't flat. Removing these outliers is a quick-fix solution to clean up the optical parameters, but it does not handle the problem of why they appear in the first place. This could be further investigated in future

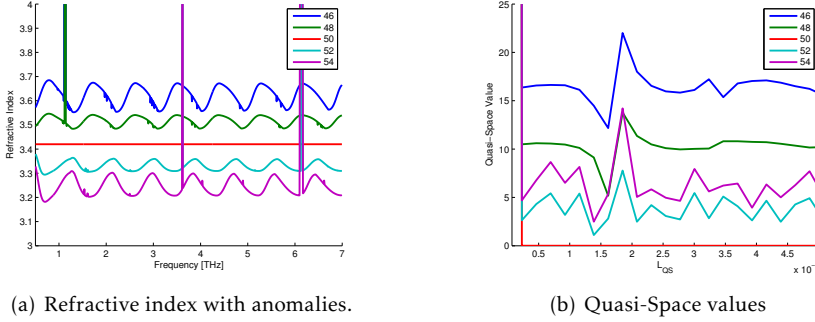


FIGURE 7.1: Anomalies in the form of spikes in the refractive index causes an increase in the Quasi-Space values

work.

7.1.1 Choice of initial guess

The error-minimization method is very dependent on where it begins searching for a minimum. In many cases, simply beginning to search for the minimum at the initial guess depending on the delay of the sample pulse is not enough, see eq. (3.11). What might work better is to use the initial guess for the first discrete frequency within the bandwidth, ω_j , and thereafter use the value that was found, $n(\omega_j)$, as the initial guess for determining the refractive index of the next frequency, $n(\omega_{j+1})$. However, if the minimization method fails to converge and causes a spike in the refractive index, that value becomes an extremely bad initial guess for the calculation of the next refractive index, $n(\omega_{j+1})$. This causes the errors to reach extreme values. The initial guess for $\kappa(\omega)$ following eq. (3.13) turned out to work well compared to a guess of zero absorption or using the value found for the previous frequency.

7.2 Measured samples

In this section, we discuss the results of the measurements of the silicon samples. We begin by making a few general remarks before we discuss the results of each individual sample. It is clear from Figs. 6.6 and 6.12 that the Nelder-Mead method does a very good job of minimizing the phase and amplitude errors. For the most part, the numerical transfer function lies on top of the measured transfer function. The restriction $\kappa \geq 0$ ensures

that the transfer function does not become greater than 1. In all cases, the determined thickness is thicker than the expected values.

Including or excluding the Fabry-Pérot reflections of the electro-optic crystal did not appear to have any quantifiable effect on the determination of the optical parameters. The differences, if any, lie in the fact that the longer measurement has a higher frequency resolution. The Fabry-Pérot reflections from the EO crystal are removed by the transfer function

$$H(\omega) = \frac{E_{sam}(\omega)FP(\omega)_{crystal}}{E_{ref}(\omega)FP(\omega)_{crystal}} = \frac{E_{sam}(\omega)}{E_{ref}(\omega)}. \quad (7.1)$$

It might be worth noting that the safest course would be to included the same amount of crystal reflections for both the reference and the sample pulse.

7.2.1 50 micron silicon sample

According to the manufacturer, the sample was 50 μm thick. However, both the Quasi-Space method and the Total Variation method find clear minima for the oscillations at thicknesses 64.3 μm . The peaks of the transfer functions shown in Fig. 6.3 very nearly reach up to 1, as we would expect from a non-absorbing Fabry-Pérot etalon. The optical parameters are far from the expected values. To summarize; nothing is as we expected. Since the minimization and thickness-determination methods work for the simulations, the problem must lie within the measurement. The sample was measured with a digital micrometer screw and was found to be 60 microns. The accuracy of the micrometer screw is only in the tens of microns, so this result is not particularly telling, but it allows that the sample could be thicker than the 50 microns claimed by the manufacturer. However, this does not account for the optical parameters being far off from the expected values. According to the manufacturer, the silicon wafer has an affinity to stick to smooth metal fixtures and jigs, glass and silicon wafers, and other surfaces. It was observed that the wafer did stick to one of the sample holders, which was subsequently exchanged. The sample was not observed to be sticking to the new sample holder, but neither were there observed any changes in the measurements. The pulse and corresponding spectrum shown in Figs. 6.1 and 6.2 are from measurements where the sample was not observed to be sticking to the holder. This sticking could be a result of surface charges, which have not been taken into account in the calculations. The 2 and 10 micron samples were delivered with an outer ring of another material. This outer ring was a few millimeters thick, which made it possible to pick up the wafers without damaging them. These samples did not stick to the holder

that the thicker sample stuck itself to. Another thing to take into account is that the sample was only polished on one side. There might have been some scattering from the rough-sided surface. In all the measurements, the THz entered the material from the smooth side. The surface roughness could possibly explain why the results were not as expected.

7.2.2 10 micron silicon sample

For the measured 10 μm silicon sample, the optical parameters are oscillating very strongly. This indicates that the thickness determined by the Quasi-Space values is incorrect. It is clear from Fig. 6.9 that the measured transfer function, even though it is very noisy, coincides well with the transfer function that is expected from the sample. For some reason the numerical fit does not overlap with the measured transfer function over a wide frequency range from 4.5 to 6 THz. For the other measurements there may be some variations between the measured and the numerical transfer functions, but nothing on this scale. Reducing the tolerance of the error minimization function did not affect the outcome. We have already discussed the fact that the minimization method is extremely dependent on the initial guess. When measuring the sample, ten measurements were performed consecutively. This way, the drift in the system can cause a significant change in the averaged time-domain signal. This could cause the difference in the arrival time between the sample and reference pulses to change. The arrival time determines the initial guess of the refractive index, which, as we already discussed, is very important. A solution to this problem could be to alternate between measuring the sample and the reference pulse and then average each group.²⁸

7.2.3 2 micron silicon sample

For the 2 μm sample, the thickness was found to be 3.6 μm . Figure 6.12 shows that the measurement is very noisy. All these fluctuations due to noise add to the variations in the optical parameters, making it harder to determine the correct thickness. This might explain why the thickness couldn't be determined correctly. On the other hand, it is implied by eq. (3.18) that the minimum detectable optical thickness is limited by the measurement bandwidth. For the measurement of the 2-micron sample, the time-delay between the pulses was approximately 0.33 fs, which when setting $l = 2\mu\text{m}$ in eq. (3.11) results in an initial guess for the refractive index, $n_{\text{guess}} \approx 6$. This is quite a bit higher than the expected value of 3.42. It could possibly be explained by drift in the system that we discussed for the 10 μm sample. The estimated value for L_{min} for the input value of $l = 2\mu\text{m}$ and

the corresponding time-delay and initial guess value is $L_{min} = 3.62\mu\text{m}$. The optical thickness of the sample should in theory be $3.42 \cdot 2\mu\text{m} = 6.84\mu\text{m}$, so it should be detectable. The fact that we are able to come within 0.2 microns of determining the thickness of the simulated $2\mu\text{m}$ sample strengthens this argument. The error in determining the thickness might be a result of the fact that the simulation has some dispersion, and the optical parameters seem to oscillate more for thin samples, which makes it harder to determine the sample thickness.

7.3 Simulations

From the results in section 6.2 we have learned two things. First of all, that the simulation has been implemented in a satisfying way. There is very little of both absorption and dispersion for the simulation of the absorptionless, dispersionless media. For the resonant media, the forms of the optical parameters fit very well with what was expected. Secondly, the algorithm for extracting the optical parameters works very well, even for media with more complex optical constants. The determined thicknesses for all kinds of media were within a few microns of the input value of the simulation. However, due to some minor precision issues for the simulation, the chosen thicknesses actually yielded better results for the optical parameters, with visibly less oscillations. For the simulations of the dispersive media, only the total-variation method managed to find a minimum. This could be due to the shapes of the optical parameters for the resonant media causing unexpected peaks in Quasi-Space.

Chapter 8

Conclusion and further work

In this thesis, a study has been made of terahertz time-domain spectroscopy of thin samples. An iterative minimalization scheme using the Nelder-Mead Simplex method has been used to find a numerical fit that corresponds well with the measured transfer function. The Nelder-Mead simplex method is used in the MATLAB function 'fminsearch'. It clearly has some issues that causes it to fail in determining the correct values for n and κ , instead causing it to find values that cannot be physically explained. This effect seems to be independent of noise since it appears for a purely analytical transfer function. There is a clear potential for improvements of the minimization method used, so that the spikes in the otherwise sinusoidal shapes of the optical parameters can be avoided.

Different methods for determining the correct sample thickness have been investigated. The bandwidth of the system determines the minimum determinable thickness, but it does not seem to be the limiting factor on the measurements performed here. For the measurements performed in this thesis, the determined thicknesses were all larger than the expected values. The different methods of determining the thickness do not always agree with each other, nor do they always find any thickness at all. These values are usually the thicknesses for which the oscillations are at a minimum, which is exactly what they should be. However, the calculated optical parameters are quite far from the expected values. This is most likely due to surface roughness, which reduces the refractive index of the medium. The scattered frequencies are interpreted as absorption. Other ways of determining the thickness, e.g. by measuring with an electron microscope could of course work, but would in any case also lead to oscillating optical parameters if the surface is rough.

There are some issues when performing measurements, e.g. in laser drift and humidity. The drift issue could be remedied by alternately measuring the sample and reference pulses instead of measuring them consecutively. An instrument that allows a more precise determination of the humidity could help indicate which measurements will influence the averaged value in a negative way. Removing noise with temporal windowing or by filtering or smoothing of the transfer function could also be looked into.

The finite-difference time-domain simulations do a good job in simulating both simple and complex media. It was observed that by interpolating the measured input pulse, the accuracy of the simulation could be increased, but when trying to interpolate the pulse further, the simulation did not work. Finding the cause of this, and possibly solving it, could result in an even more precise simulation. A natural expansion of the simulation could include media with more than one resonance.

Appendix A

The Nelder-Mead Simplex method

The Nelder-Mead simplex-reflection method, named after its authors John Nelder and Roger Mead, is a derivative free optimization method used to find extreme values of a function in multi-dimensional space.³¹ In n -dimensional space, \mathbb{R}^n , we keep track of $n + 1$ points, whose convex hull form a simplex. The simplest way to visualize this is by considering a triangle in a two-dimensional space as shown in Fig. A.1. Through one iteration of the algorithm we attempt to replace the vertex with the worst function value with another vertex with a better value. The new point is obtained by one of four different steps; reflection, extraction or inner or outer contraction along the line joining the worst vertex with the centroid of the remaining vertices. If none of these work, we retain only the vertex with the best function value and shrink the simplex by moving all the other vertices closer to this one. One iteration of the algorithm follows this procedure:

Step 1: Sort the vertices so that.

$$f(x_1) \leq f(x_2) \leq \dots \leq f(x_{n+1}). \quad (\text{A.1})$$

Step 2: Calculate the centroid \bar{x} of all points except x_{n+1} . The centroid is defined as,

$$\bar{x} = \sum_{i=1}^n x_i. \quad (\text{A.2})$$

Step 3: Calculate the values of points along the line joining \bar{x} and the worst vertex x_{n+1} . Let the centroid be the origin and the distance between the \bar{x} and x_{n+1} is 1. The line is denoted by

$$\bar{x}(t) = \bar{x} + t(x_{n+1} - \bar{x}). \quad (\text{A.3})$$

We see that $\bar{x}(1) = x_{n+1}$. The algorithm replaces the worst vertex and returns to step 1 until the extreme value has been found. The replacement vertex is found by finding the *reflection* point and calculating its function value.

The reflection point is located along the line $\bar{x}(t)$, the same distance from the centroid as the worst vertex, but on the opposite side:

$$\bar{x}_r = \bar{x}(-1). \quad (\text{A.4})$$

If the function value $f(\bar{x}_r)$ is less than or equal to the function value at the second worst vertex and worse than or equal to the best vertex, i.e. $f(x_1) \leq f(\bar{x}_r) \leq f(x_n)$ then \bar{x}_r replaces the worst vertex, and the algorithm returns to step 1, where we sort the vertices by their function values. Note that if we were to compare \bar{x}_r with x_{n+1} and they turned out to be equal, we could end up reflecting back and forth infinitely. Therefore we compare to the second worst vertex x_n . There are two possibilities if the reflection conditions are not met. For the case where the function value at the reflection point is less than that of the best vertex, i.e. $f(\bar{x}_r) < f(x_1)$, we want to continue in the same direction. We calculate the *expansion* point

$$\bar{x}_e = \bar{x}(-2), \quad (\text{A.5})$$

which is in the same direction as the reflection point, but twice the distance from the centroid. If $f(\bar{x}_e) < f(\bar{x}_r)$, we exchange x_{n+1} with \bar{x}_e . If this is not the case, but the condition $f(\bar{x}_r) \leq f(x_n)$ is still the case, then the reflection point still becomes the new vertex. In the second scenario, the reflection point actually turns out to be worse than the worst vertex. We then calculate the *outer contraction* point $\bar{x}_{oc} = \bar{x}(-1/2)$. If $f(\bar{x}_{oc}) < f(\bar{x}_r)$ this becomes the new vertex. If not, we find the *inner contraction* point, $\bar{x}_{ic} = \bar{x}(1/2)$. This point becomes the new vertex if it is better than the worst vertex ($f(\bar{x}_{ic}) < f(\bar{x}_{n+1})$).

Step 4: If none of these conditions are met, i.e. we cannot find a vertex to exchange with the worst one, we shrink the simplex towards the best vertex x_1 , so that

$$x_i = \frac{1}{2}(x_1 + x_i), i = 2, 3, \dots, n + 1. \quad (\text{A.6})$$

After the new vertex has been found or the simplex has been shrunk, the process is repeated for the new simplex.

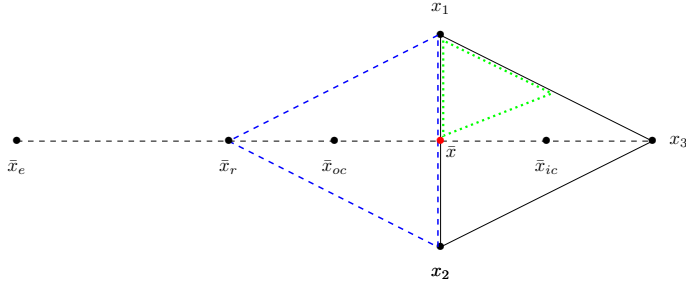


FIGURE A.1: The Nelder-Mead simplex in \mathbb{R}^2 . The simplex is spanned by the solid, black line between the vertices x_1, x_2 and x_3 . The dashed, black line represents $\bar{x}(t)$, which passes through the centroid, \bar{x} marked in red, and the worst vertex x_3 . The points of reflection, expansion and contraction lie along this line. The blue triangle represents the new simplex generated by reflection and the green triangle represents the new simplex generated by shrinking the simplex.

Appendix B

An interesting phenomenon

When a THz pulse is generated, something interesting happens. A much smaller pulse appears some time before the actual pulse. Figure B.1 shows two THz pulses. One was created by an air-plasma interaction in the setup at NTNU used in this thesis. It was detected by an electro-optic crystal. The other pulse was generated with a photoconductive antenna at a setup at Forsvarets Forskningsinstitut (FFI) and was taken as a part of another project. It was detected by a photconductive switch. Even though the setups are very different, they both exhibit this phenomena. For the plasma-generated pulse, the difference in arrival time for the pre-pulse and the main pulse is within half a picosecond of the period between reflections from the electro-optic crystal.

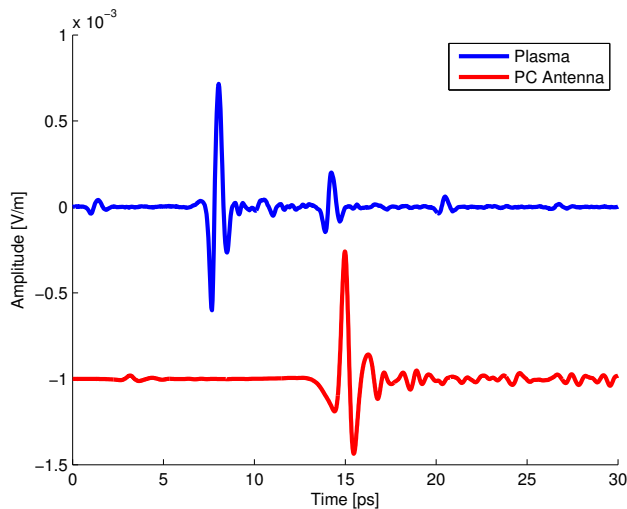


FIGURE B.1: THz pulses created by air-plasma interaction and photoconductive antenna. The photoconductive pulse propagated through non-dry air, and is therefore very noisy.

Figure B.2 shows a zoomed in image of the pre-pulses. We can see that they have close to the same shape as the main-pulses.

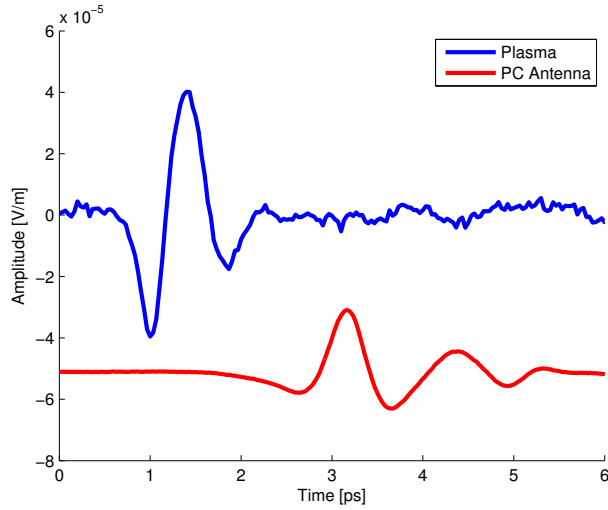


FIGURE B.2: Zoomed in image of the pre-pulses.

Even though the pre-pulse appears for different experimental setups, a search for articles that mention it has so far not yielded any results. The time-windows for the measurements are usually adjusted so as to exclude the pre-pulse..

Appendix C

Sign conventions

Electrical engineers and physicists do not agree on whether a propagating wave should be expressed as $E^{i(\omega t - \vec{k}\vec{r})}$ or $E^{i(\vec{k}\vec{r} - \omega t)}$. The complex refractive index is expressed as $\hat{n} = n - i\kappa$ or $\hat{n} = n + i\kappa$, respectively. The condition $\kappa \geq 0$ holds in both cases. The difference causes some signs to change, e.g. in the expressions for the Lorentz and Debye media.

Bibliography

- [1] H.-B. Liu and Y. Chen. "Detection and identification of explosive RDX by THz diffuse reflection spectroscopy".
In: *Optics Express* 14.1 (2006), pp. 415–423 (cit. on p. 1).
- [2] M.-A. Brun, F. Formanek, A. Yasuda, M. Sekine, N. Ando, and Y. Eishii. "Terahertz imaging applied to cancer diagnosis".
In: *Physics in medicine and biology* 55 (2010), pp. 4615–4623 (cit. on p. 1).
- [3] F. Matsushima, H. Odashima, T. Iwasaki, S. Tsunekawa, and K. Takagi. "Frequency measurement of pure rotational transitions of H₂O from 0.5 to 5 THz".
In: *Journal of Molecular Structure* 352/353 (1995), pp. 371–378 (cit. on p. 1).
- [4] M. Schall, M. Walther, and P. Jepsen. "Fundamental and second-order phonon processes in CdTe and ZnTe". In: *Physical Review B* 64 (2001) (cit. on p. 1).
- [5] R. W. Boyd. *Principles of Nano-Optics*. 3rd ed. Academic Press, 2008. ISBN: 978-0-12-369470-6 (cit. on p. 3).
- [6] Y.-S. Lee. *Principles of Terahertz Science and Technology*. Springer, 2009. ISBN: 978-0-387-09539-4 (cit. on p. 3).
- [7] Y. B. Band. *Light and Matter - Electromagnetism, Optics, Spectroscopy and Lasers*. John Wiley & Sons Ltd, 2007. ISBN: 0-471-89931-3 (cit. on p. 9).
- [8] J. T. Kindt and C. A. Schmuttenmaer. "Far-Infrared Dielectric Properties of Polar Liquids Probed by Femtosecond Terahertz Pulse Spectroscopy".
In: *J. Phys. Chem.* 24.100 (1996), 10373–10379 (cit. on p. 11).
- [9] *photonicswiki Terahertz Radiation, Creative Commons - Attribution Non-Commercial Share Alike (cc by-nc-sa)*. http://photonicswiki.org/index.php?title=Terahertz_Radiation. Accessed: 2015.06.16 (cit. on pp. 15, 17, 20).
- [10] H. Hamster, A. Sullivan, S. Gordon, W. White, and R. W. Falcone. "Subpicosecond, Electromagnetic Pulses from Intense Laser-Plasma Interaction". In: *Physical Review Letters* 71.17 (1993), pp. 2725–2728 (cit. on p. 18).

- [11] D. J. Cook and R. M. Hochstrasser.
“Intense terahertz pulses by four-wave rectification in air”.
In: *Optics Letters* 25.16 (2000), pp. 1210–1212 (cit. on p. 18).
- [12] D. Mittleman. *Sensing with Terahertz Radiation*. Springer, 2003.
ISBN: 3-540-43110-1 (cit. on p. 20).
- [13] J.-C. Diels and W. Rudolph. *Ultrashort Laser Pulse Phenomena*. 2nd ed.
Academic Press, 2006. ISBN: 978-0-12-215493-5 (cit. on p. 24).
- [14] L. Duvillaret, F. Garet, and J.-L. Coutaz.
“A reliable Method for Extraction of Material Parameters in Terahertz Time-Domain Spectroscopy”. In: *IEEE Journal of selected topics in quantum electronics* 2.3 (1996), pp. 739–746
(cit. on pp. 24, 26, 39, 43).
- [15] R. Trebino. *Frequency-Resolved Optical Gating: The Measurement of Ultrashort Laser Pulses*. Kluwer Academic Publisher, 2000.
ISBN: 1-4020-7066-7 (cit. on p. 24).
- [16] P. U. Jepsen, D. G. Cooke, and M. Koch. “Terahertz spectroscopy and imaging - Modern techniques and applications”.
In: *Laser and Photonics Reviews* 5.1 (2011), pp. 124–166 (cit. on p. 25).
- [17] L. Duvillaret, F. Garet, and J.-L. Coutaz.
“Highly precise determination of optical constants and sample thickness in terahertz time-domain spectroscopy”.
In: *Applied Optics* 38.2 (1999), pp. 409–415 (cit. on pp. 25, 26, 40, 43).
- [18] T. D. Dorney, R. G. Baraniuk, and D. M. Mittleman. “Material parameter estimation with terahertz time-domain spectroscopy”.
In: *J. Opt. Soc. Am. A* 18.7 (2001), pp. 1532–1571
(cit. on pp. 26, 27, 43).
- [19] W. Withayachumnankul, B. Ferguson, T. Rainsford, S. P. Micken, and D. Abbott. “Material parameter extraction for terahertz time-domain spectroscopy using fixed-point iteration”.
In: *SPIE* 5840 (2005), pp. 221–231 (cit. on p. 26).
- [20] I. Pupeza, R. Wilk, and M. Koch. “Highly accurate optical material parameter determination with THz time-domain spectroscopy”.
In: *Optics Express* 15.7 (2007), pp. 4335–4350
(cit. on pp. 26, 27, 40, 43).
- [21] M. Scheller, C. Jansen, and M. Koch. “Analyzing sub-100- μm samples with transmission terahertz time domain spectroscopy”.
In: *Optics Communication* 282 (2009), pp. 1304–1306
(cit. on pp. 26, 28, 43).

- [22] W. Tu, S.-C. Zhong, H.-Z. Yao, and Y.-C. Shen.
“FDTD-based computed terahertz wave propagation in multilayer medium structures”. In: *SPIE* 8909 (2013) (cit. on p. 31).
- [23] A. Fitzgerald, E. Pickwell-MacPherson, and V. Wallace.
“Use of Finite Difference Time Debye Theory for Modelling the Terahertz Reflection Response of Normal and Tumour Breast Tissue”. In: *PLOS ONE* 9.7 (2014) (cit. on p. 31).
- [24] A. Taflove. *Computational Electrodynamics - The Finite Difference Time Domain Method*. Artech House, Inc., 1995. ISBN: 0-89006-792-9 (cit. on p. 31).
- [25] A. Bondeson, T. Rylander, and P. Ingelström.
Computational Electromagnetics. Springer, 2005. ISBN: 0-387-26158-3 (cit. on p. 31).
- [26] A. Wojdyla and G. Gallot.
“Brewster’s angle silicon wafer terahertz linear polarizer”. In: *Optical Express* 19.15 (2011), pp. 14099–14107 (cit. on p. 38).
- [27] M. Krüger, S. Funkner, E. Bründermann, and M. Havenith.
“Uncertainty and Ambiguity in Terahertz Parameter Extraction and Data Analysis”. In: *Journal of Infrared, Millimeter, and Terahertz Waves* 32 (5 2011), pp. 699–715 (cit. on pp. 40, 43).
- [28] W. Withayachumnankul, J. O’Hara, W. Cao, I. Al-Naib, and W. Zhang.
“Limitation in thin-film sensing with transmission-mode terahertz time-domain spectroscopy”. In: *Optics Express* 22.1 (2014), pp. 973–986 (cit. on pp. 40, 58).
- [29] M. Naftaly and R. Dudley.
“Methodologies for determining the dynamic ranges and signal-to-noise ratios of terahertz time-domain spectrometers”. In: *Optics Letters* 15.8 (2009), pp. 1213–1215 (cit. on p. 41).
- [30] P. U. Jepsen and B. M. Fischer. “Dynamic range in terahertz time-domain transmission and reflection spectroscopy”. In: *Optics Letters* 30.1 (2005), pp. 29–31 (cit. on p. 41).
- [31] J. Nocedal and S. J. Wright. *Numerical Optimization*. 2nd ed. Springer, 2006. ISBN: 0-387-30303-0 (cit. on p. 63).